ANNUAL REVIEWS

*Annual Review of Fluid Mechanics*

# Immersed Methods for Fluid–Structure Interaction

Boyce E. Griffith[1] and Neelesh A. Patankar[2]

[1]Departments of Mathematics, Applied Physical Sciences, and Biomedical Engineering, University of North Carolina, Chapel Hill, North Carolina 27599, USA; email: boyceg@email.unc.edu

[2]Department of Mechanical Engineering, Northwestern University, Evanston, Illinois 60208, USA; email: n-patankar@northwestern.edu

Annu. Rev. Fluid Mech. 2020. 52:421–48

First published as a Review in Advance on September 5, 2019

The *Annual Review of Fluid Mechanics* is online at fluid.annualreviews.org

https://doi.org/10.1146/annurev-fluid-010719-060228

Copyright © 2020 by Annual Reviews. All rights reserved

ANNUAL REVIEWS CONNECT

www.annualreviews.org

- Download figures
- Navigate cited references
- Keyword search
- Explore related articles
- Share via email or social media

## Keywords

fluid–structure interaction, immersed boundary method, immersed interface method, immersed finite-element method, applications in medicine and biology

## Abstract

Fluid–structure interaction is ubiquitous in nature and occurs at all biological scales. Immersed methods provide mathematical and computational frameworks for modeling fluid–structure systems. These methods, which typically use an Eulerian description of the fluid and a Lagrangian description of the structure, can treat thin immersed boundaries and volumetric bodies, and they can model structures that are flexible or rigid or that move with prescribed deformational kinematics. Immersed formulations do not require body-fitted discretizations and thereby avoid the frequent grid regeneration that can otherwise be required for models involving large deformations and displacements. This article reviews immersed methods for both elastic structures and structures with prescribed kinematics. It considers formulations using integral operators to connect the Eulerian and Lagrangian frames and methods that directly apply jump conditions along fluid–structure interfaces. Benchmark problems demonstrate the effectiveness of these methods, and selected applications at Reynolds numbers up to approximately 20,000 highlight their impact in biological and biomedical modeling and simulation.

## 1. INTRODUCTION

Fluid–structure interaction is ubiquitous in nature. It occurs at every biological length scale, from the writhing of DNA in nucleoplasm to the beating of cilia and flagella and the projection of lamellipodia and bleb-like protrusions by motile cells, the flow of blood in the heart and throughout the circulation, swimming fish and flying birds and insects, and the dispersal of seeds and pollen by the wind. Many of these systems can be described as elastic structures immersed in viscous incompressible fluids. A challenge in simulating these systems is that the fluid–structure interface can be subject to large deformations and displacements. Mathematical descriptions that use partitioned descriptions of the fluid and structure can be approximated using separate, nonoverlapping meshes for the fluid and solid regions, as in arbitrary Lagrangian–Eulerian methods (Donea et al. 1982, Hu et al. 2001, Bazilevs et al. 2008), and these body-fitted formulations yield excellent resolution of the flows and stress distributions along the interface between the fluid and the structure. However, body-fitted methods can require frequent remeshing that can limit their feasibility for models involving very large deformations, thin structures, or transient contact.

The immersed formulation of fluid–structure interaction offers an alternative to body-fitted approaches. These methods use overlapping descriptions of the fluid and structure. It is common for them to describe the fluid in Eulerian form and the structure in Lagrangian form, and to use nonconforming discretizations along the fluid–structure interface. Immersed methods can thereby avoid many of the difficulties of mesh regeneration encountered in body-conforming discretizations. The key challenge in developing immersed methods, however, is the coupling operators that link the Eulerian and Lagrangian variables.

An earlier review in this journal by Mittal & Iaccarino (2005) also described immersed methods. Its major focus was on methods for treating stationary and rigid-body models. In the intervening years, the popularity of immersed methods for fluid–structure interaction has continued to grow. Here we concentrate on formulations and applications of fluid–structure interaction involving immersed elastic structures and structures with prescribed kinematics, which includes rigid bodies as a special case. The methods that we detail are primarily related to an approach introduced by Peskin (1972, 1977) that is now known as the immersed boundary method (Peskin 2002). Peskin's approach couples the Eulerian and Lagrangian frames through integral transforms with Dirac delta function kernels, and numerical treatments of this formulation often replace these singular kernels with regularized delta functions. Immersed methods that use regularized delta function kernels are straightforward to implement but appear to be limited to lower-order accuracy at fluid–structure interfaces because they smooth stress discontinuities that generically occur along such interfaces. In addition, these methods can yield slowly converging force distributions along the fluid–structure interface. We also describe immersed interface methods for the incompressible Navier–Stokes equations (Li & Lai 2001, Kolahdouz et al. 2019), which can improve accuracy in velocity, deformation, and stresses by avoiding regularized kernels, although they also require coupling algorithms that involve more complex geometrical computations than conventional immersed boundary methods. We outline approaches to modeling elastic structures with these methods, including fiber-based elasticity models and finite-strain continuum mechanics formulations that are well suited for finite-element structural models. Immersed methods have also been developed that use the framework of isogeometric analysis (Hughes et al. 2005), including methods developed by Hsu et al. (2014, 2015), Kamensky et al. (2015), and Casquero et al. (2018).

In some cases, it is desirable or even necessary to develop models of deforming structures without a fully detailed mechanics model. For instance, some models of fish swimming for understanding neuromuscular coupling may require detailed descriptions of the underlying physiology, but models that seek to understand the impact of a particular gait on swimming efficiency may not.

To treat the latter case, we also discuss closely related distributed Lagrange multiplier methods, which were originally introduced by Glowinski, Patankar, and coworkers (Glowinski et al. 1998, 1999; Patankar et al. 2000) for immersed rigid structures.

Another advantage of the present immersed formulations is that they do not appear to suffer from instabilities related to the added mass effect, even when explicit coupling strategies are used to link the Eulerian and Lagrangian variables. A challenge in using explicit coupling strategies, however, is that applications that involve stiff elastic structures or penalty methods with large penalty parameter values require small time steps. These time step size restrictions can be eliminated by adopting implicit coupling methods, but the efficient solvers demanded by these approaches are still lacking for many practical cases of interest and remain a topic of ongoing research.

This paper includes examples showing the performance of the methodology at Reynolds numbers as high as approximately 20,000. There does not appear to be a fundamental limitation in using these methods in higher Reynolds number applications given adequate computing resources. Efficiently treating such problems, however, motivates future research on developing suitable turbulence modeling capabilities into the framework described herein.

Other immersed methods have been developed for modeling fluid–structure interaction and flows in complex geometries. These include the immersed boundary methods of Ye et al. (1999), Fadlun et al. (2000), Udaykumar et al. (2001), Iaccarino & Verzicco (2003), Gilmanov & Sotiropoulos (2005), Mittal et al. (2008), and Borazjani et al. (2008). Many of these are sharp-interface immersed boundary methods that modify the finite-difference stencils near the immersed boundary to ensure an accurate representation of the fluid boundary layer. Typically they consider the immersed boundary to be a boundary of the flow domain and will solve the equations of fluid dynamics on only one side of the interface. This is in contrast to the approaches that are the focus of this review, which model structures that are completely immersed in fluid.

## 2. MODEL FORMULATIONS

### 2.1. Interfacial Models

Consider an infinitesimally thin elastic boundary or interface that is immersed in a viscous incompressible fluid (**Figure 1*a***). We assume that the interface is massless and that the fluid is incompressible and has uniform density $\rho$ and uniform dynamic viscosity $\mu$. The mathematical formulation and numerical methods can be extended to variable-density and variable-viscosity

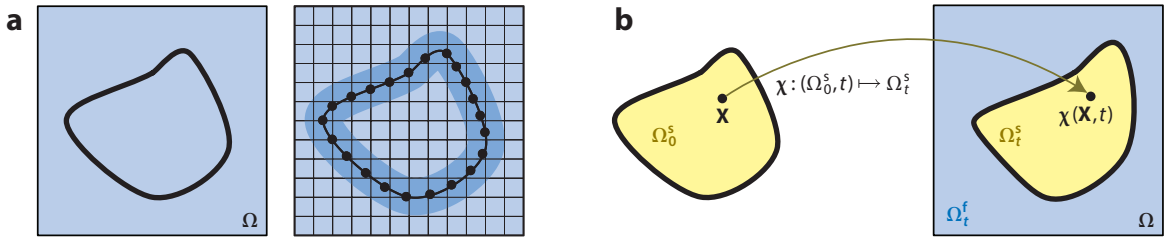


**Figure 1**

(*a*) An immersed boundary in the domain $\Omega$ (*left*) and potential corresponding Eulerian and Lagrangian discretizations (*right*). In formulations that use a regularized delta function, forces are applied in a region with finite thickness about the interface, and velocities are interpolated to the interface from the same region. (*b*) In volumetric formulations, the coordinate mapping $\boldsymbol{\chi}$ connects reference coordinates $\mathbf{X} \in \Omega_0^s$ to current coordinates $\mathbf{x} \in \Omega_t^s$.

fluid models (Fai et al. 2013, 2014; Nangia et al. 2019) and to thin interfaces with mass (Zhu & Peskin 2002, Kim et al. 2003, Kim & Peskin 2007).

We take the fluid to occupy a fixed region $\Omega \subset \mathbb{R}^3$, and we let $\mathbf{x} = (x_1, x_2, x_3) \in \Omega$ be physical coordinates. The fluid is described in Eulerian form in terms of its velocity, $\mathbf{u}(\mathbf{x}, t)$, and hydrostatic pressure, $p(\mathbf{x}, t)$. The interface is described in Lagrangian form using curvilinear coordinates, $\mathbf{q} = (q_1, q_2) \in U \subset \mathbb{R}^2$, attached to the structure. The expression $\boldsymbol{\chi}(\mathbf{q}, t) \in \Omega$ indicates the physical position of material point $\mathbf{q}$ at time $t$, and $\Gamma_t = \boldsymbol{\chi}(U, t)$ is the position of the interface at time $t$. A force density $\mathbf{F}(\mathbf{q}, t)$ is applied by the interface to the fluid, such that $\mathbf{F}(\mathbf{q}, t)\, d\mathbf{q}$ is the total force applied by surface patch $d\mathbf{q}$. We assume that the no-slip condition holds between the fluid and the interface, although extensions to porous interfaces relax the no-slip condition along the boundary (Stockie 2009).

**2.1.1. Integral formulation.** The immersed boundary method (Peskin 2002) uses integral equations with Dirac delta function kernels to couple the Eulerian and Lagrangian variables,

$$\rho \frac{D\mathbf{u}}{Dt}(\mathbf{x}, t) = -\nabla p(\mathbf{x}, t) + \mu \nabla^2 \mathbf{u}(\mathbf{x}, t) + \mathbf{f}(\mathbf{x}, t), \tag{1.}$$

$$\nabla \cdot \mathbf{u}(\mathbf{x}, t) = 0, \tag{2.}$$

$$\mathbf{f}(\mathbf{x}, t) = \int_U \mathbf{F}(\mathbf{q}, t)\, \delta[\mathbf{x} - \boldsymbol{\chi}(\mathbf{q}, t)]\, d\mathbf{q}, \tag{3.}$$

$$\frac{\partial \boldsymbol{\chi}}{\partial t}(\mathbf{q}, t) = \int_\Omega \mathbf{u}(\mathbf{x}, t)\, \delta[\mathbf{x} - \boldsymbol{\chi}(\mathbf{q}, t)]\, d\mathbf{x}, \tag{4.}$$

in which $U$ is the curvilinear coordinate domain, $D/Dt = \partial/\partial t + \mathbf{u}(\mathbf{x}, t) \cdot \nabla$ is the convective derivative, and $\delta(\mathbf{x}) = \prod_{i=1}^{3} \delta(x_i)$ is the three-dimensional Dirac delta function. Section 2.1.3 discusses a specific force model that has been used with the method, but this formulation is amenable to any structural model using positional degrees of freedom along a material surface, such as the center surface of a thin shell (Eggleton & Popel 1998, Givelberg 2004, Fai et al. 2013, Le 2010, Maxian et al. 2018). Shell theories for thin elastic structures that include rotational degrees of freedom such as director vectors (Bischoff et al. 2004) would require an extension to this formulation similar to the method developed by Lim et al. (2008) for immersed rods.

It is important to notice that in this formulation, the Eulerian elastic force density $\mathbf{f}(\mathbf{x}, t)$ is not a regular function. Instead, it is a distribution with a singular force layer concentrated along the current configuration of the immersed boundary, $\Gamma_t$. Nonetheless, the defining property of the Dirac delta function implies that $\mathbf{f}(\mathbf{x}, t)$ and $\mathbf{F}(\mathbf{q}, t)$ are equivalent as distributions (Peskin 2002). Because the fluid is viscous, $\mathbf{u}(\mathbf{x}, t)$ is continuous on $\Omega$, and the defining property of the delta function also implies that Equation 4 is equivalent to $\frac{\partial \boldsymbol{\chi}}{\partial t}(\mathbf{q}, t) = \mathbf{u}[\boldsymbol{\chi}(\mathbf{q}, t), t]$, which is the immersed boundary form of the no-slip condition (Peskin 2002).

Some methods for Equations 1–4 replace the singular delta function by a smoothed delta function, $\delta_\epsilon(\mathbf{x})$, in which $\epsilon$ is a regularization parameter (**Figure 1*a***). The construction of $\delta_\epsilon(\mathbf{x})$ is tied to the details of the spatial discretization, but typically $\epsilon$ is chosen to be linearly proportional to $h$, where $h$ characterizes the Eulerian grid spacing. This allows the regularization to act over a distance that is comparable to the fluid grid spacing and recovers the singular formulation as $h \downarrow 0$.

**2.1.2. Jump condition formulation.** The force applied by a thin boundary to the fluid will induce discontinuities in the fluid traction along the interface, and it is possible to rewrite

Equations 1–4 in terms of jump conditions for the pressure and normal shear stress that must be satisfied along the immersed boundary (Peskin & Printz 1993, Lai & Li 2001). Discretizing these equations leads to the immersed interface method, which was first developed as a numerical method for the incompressible Navier–Stokes equations by Li & Lai (2001).

Let $[\![c(\mathbf{x}^\star,t)]\!]$ denote the value of a discontinuity in an Eulerian field $c(\mathbf{x},t)$ at $\mathbf{x}^\star \in \Gamma_t$. Discontinuities in the fluid stress along the interface balance the applied interfacial force, $[\![\sigma\mathbf{n}]\!] = \mathbf{F}/\left\| \frac{\partial \mathbf{X}}{\partial q_1} \times \frac{\partial \mathbf{X}}{\partial q_2} \right\|$, which can be directly related to jump conditions for $p$ and $\partial\mathbf{u}/\partial\mathbf{n}$. Xu & Wang (2006b) systematically derived successively higher-order jump conditions from these low-order jump conditions. In practice, it is necessary to consider only a finite number of interface conditions, and effective numerical schemes can be developed that use only the lowest-order jump conditions (Kolahdouz et al. 2019). Methods can also be developed that use higher-order jump conditions (Li & Lai 2001; Xu & Wang 2006a, 2008).

**2.1.3. Membrane mechanics.** Many models by Peskin and coworkers describe the structural mechanics in terms of a strain energy functional $E = E[\mathbf{X}(\cdot,t)]$ that is associated with the total energy of the structural configuration (Peskin 2002). The corresponding Lagrangian elastic force density is obtained by taking the total (Fréchet) derivative of $E$ with respect to the deformation. It is straightforward to use this approach to model a fiber-reinforced membrane. Assume that the Lagrangian coordinates $\mathbf{q} = (q_1, q_2)$ have been constructed so that $q_1$ labels a fiber and $q_2 \mapsto \mathbf{X}(q_1^\star, q_2)$ is a parametric description of the particular fiber labeled by $q_1^\star$. We obtain the global energy $E$ from local stretching energies $\mathcal{E}$ via $E[\mathbf{X}] = \int \mathcal{E}\left(\left\| \partial\mathbf{X}/\partial q_2 \right\|\right) \mathrm{d}\mathbf{q}$, which yields $\mathbf{F} = \frac{\partial}{\partial q_2}\left[\mathcal{E}'\left(\left\| \frac{\partial \mathbf{X}}{\partial q_2} \right\|\right) \frac{\partial \mathbf{X}/\partial q_2}{\|\partial \mathbf{X}/\partial q_2\|}\right] = \frac{\partial (T\boldsymbol{\tau})}{\partial q_2}$, in which $T = \mathcal{E}'\left(\|\partial\mathbf{X}/\partial q_2\|\right)$ is the fiber tension and $\boldsymbol{\tau} = \frac{\partial \mathbf{X}/\partial q_2}{\|\partial \mathbf{X}/\partial q_2\|}$ is the unit fiber tangent vector. A particularly simple example corresponds to a generalization of a Hookean spring with a zero resting length, for which we have $T = S\left\|\partial\mathbf{X}/\partial q_2\right\|$, in which $S$ is the fiber stiffness. In this case, we have $\mathbf{F} = S\partial^2\mathbf{X}/\partial q_2^2$. This approach also accommodates nonlinear length–tension relationships, and it can treat bending through energies that depend on higher derivatives of the deformation $\mathbf{X}$ (McQueen & Peskin 2000, 2001; Griffith et al. 2007, 2009a,b; Griffith 2012). It also can be readily applied to model volumetric bodies (McQueen & Peskin 2000, 2001; Peskin 2002; Griffith & Peskin 2005; Griffith et al. 2007, 2009a). More general strain measures can also be used to describe the elasticity of the interface, as in the neo-Hookean membrane model of Evans & Skalak (1980) used by Fai et al. (2013) to simulate red blood cells. Other membrane and shell models have also been used with the immersed boundary formulation (Eggleton & Popel 1998; Le 2010; Pranay et al. 2010, 2012; Zhu & Brandt 2015; Banaei et al. 2017). Bischoff et al.'s (2004) review provides an overview of the formulation and discretization of models of thin elastic structures.

## 2.2. Volumetric Models

The formulation introduced in Section 2.1 can be extended to describe volumetric bodies immersed in fluid. Now, however, we divide $\Omega$ into fluid and solid subregions, $\Omega_t^{\mathrm{f}} \subset \Omega$ and $\Omega_t^{\mathrm{s}} \subset \Omega$, both indexed by time $t$. The fluid and solid fill $\Omega$ and meet along the fluid–solid interface $\Gamma_t^{\mathrm{fs}} = \overline{\Omega_t^{\mathrm{f}}} \cap \overline{\Omega_t^{\mathrm{s}}}$. As with an immersed boundary, we assume that the no-slip condition holds between the fluid and the structure.

**2.2.1. Eulerian and Lagrangian equations of motion.** In the formulation described here, we describe the structural kinematics in Lagrangian form using the mapping $\mathbf{X} : (\Omega_0^{\mathrm{s}}, t) \mapsto \Omega_t^{\mathrm{s}}$, which connects the reference configuration to the current configuration at time $t$ (**Figure 1*b***).

Specifically, $\boldsymbol{\chi}(\mathbf{X},t) \in \Omega_t^{\mathrm{s}}$ is the position at time $t$ of material point $\mathbf{X} \in \Omega_0^{\mathrm{s}}$. We introduce a composite material velocity field on $\Omega$ defined so that $\mathbf{u}(\mathbf{x},t)$ is the velocity of whichever material happens to be located at position $\mathbf{x}$ at time $t$. Our formulation uses the first Piola–Kirchhoff solid stress tensor $\mathbb{P}^{\mathrm{s}}$, which is related to the corresponding Cauchy stress tensor $\sigma^{\mathrm{s}}$ by $\mathbb{P}^{\mathrm{s}}(\mathbf{X},t) = J(\mathbf{X},t)\,\sigma^{\mathrm{s}}[\boldsymbol{\chi}(\mathbf{X},t),t]\,\mathbb{F}(\mathbf{X},t)^{-T}$, in which $\mathbb{F} = \partial\boldsymbol{\chi}/\partial\mathbf{X}$ is the deformation gradient tensor and $J = \det(\mathbb{F})$ is the Jacobian determinant. Constitutive models to determine $\mathbb{P}^{\mathrm{s}}$ are briefly described in Section 2.2.2.

We restrict our discussion to a neutrally buoyant, incompressible structure immersed in a viscous incompressible fluid, so that $\rho$ is the mass density of both the fluid and the solid. Further, we assume that the structure is viscoelastic and that the form of the solid viscosity is the same as that of the fluid. Under these assumptions, the immersed equations are

$$\rho\frac{\mathrm{D}\mathbf{u}}{\mathrm{D}t}(\mathbf{x},t) = -\nabla p(\mathbf{x},t) + \mu\nabla^2\mathbf{u}(\mathbf{x},t) + \mathbf{f}(\mathbf{x},t) + \mathbf{t}(\mathbf{x},t), \tag{5.}$$

$$\nabla\cdot\mathbf{u}(\mathbf{x},t) = 0, \tag{6.}$$

$$\mathbf{f}(\mathbf{x},t) = \int_{\Omega_0^{\mathrm{s}}} \nabla_{\mathbf{x}}\cdot\mathbb{P}^{\mathrm{s}}(\mathbf{X},t)\,\delta[\mathbf{x}-\boldsymbol{\chi}(\mathbf{X},t)]\,\mathrm{d}\mathbf{X}, \tag{7.}$$

$$\mathbf{t}(\mathbf{x},t) = -\int_{\partial\Omega_0^{\mathrm{s}}} \mathbb{P}^{\mathrm{s}}(\mathbf{X},t)\,\mathbf{N}(\mathbf{X})\,\delta[\mathbf{x}-\boldsymbol{\chi}(\mathbf{X},t)]\,\mathrm{d}A, \tag{8.}$$

$$\frac{\partial\boldsymbol{\chi}}{\partial t}(\mathbf{X},t) = \int_{\Omega}\mathbf{u}(\mathbf{x},t)\,\delta[\mathbf{x}-\boldsymbol{\chi}(\mathbf{X},t)]\,\mathrm{d}\mathbf{x}, \tag{9.}$$

in which $\mathbf{N}$ is the outward unit normal to $\partial\Omega_0^{\mathrm{s}}$ in the reference configuration, so that $\mathbb{P}^{\mathrm{s}}\mathbf{N}$ is the solid traction along the fluid–solid interface and $-\mathbb{P}^{\mathrm{s}}\mathbf{N}\,\mathrm{d}A$ is the traction force applied by the structure to the fluid on interfacial patch $\mathrm{d}A$. Notice that Equation 5 accounts for the momentum of both the fluid and the immersed structure. Generalizations of the thin interface methods of Zhu & Peskin (2002), Kim et al. (2003), and Kim & Peskin (2007), or variable-coefficient solvers like those of Nangia et al. (2019), can be used to treat the case in which the mass density of the structure is different from that of the fluid. The present formulation is more challenging to extend to treat a purely elastic structure, and although in principle variable-viscosity solvers could allow for the elimination of viscous stresses within the solid region, at present, this approach is not widely used in practice. Extensions have also been introduced that allow for the treatment of immersed compressible solids (Roy et al. 2015, Boffi et al. 2018).

To interpret this formulation, we define fluid and solid stress tensors throughout $\Omega$ via

$$\overline{\sigma}^{\mathrm{f}}(\mathbf{x},t) = -p(\mathbf{x},t)\mathbb{I} + \mu\left[\nabla\mathbf{u}(\mathbf{x},t) + \nabla\mathbf{u}(\mathbf{x},t)^T\right] \tag{10.}$$

and

$$\overline{\sigma}^{\mathrm{s}}(\mathbf{x},t) = \begin{cases} \mathbb{0}, & \mathbf{x}\in\Omega_t^{\mathrm{f}}, \\ \sigma^{\mathrm{s}}(\mathbf{x},t), & \mathbf{x}\in\Omega_t^{\mathrm{s}}. \end{cases} \tag{11.}$$

The composite stress is $\sigma = \overline{\sigma}^{\mathrm{f}} + \overline{\sigma}^{\mathrm{s}}$, and the right-hand side of Equation 5 is $\nabla\cdot\sigma$. In addition, the Eulerian force density $\mathbf{f}$ is equivalent as a density to $\mathbf{F} = \nabla_{\mathbf{x}}\cdot\mathbb{P}^{\mathrm{s}}$, and we have

$$\mathbf{f}(\mathbf{x},t) = \begin{cases} \mathbf{0}, & \mathbf{x}\in\Omega_t^{\mathrm{f}}, \\ J^{-1}(\mathbf{X},t)\,\mathbf{F}(\mathbf{X},t), & \mathbf{x}\in\Omega_t^{\mathrm{s}}, \end{cases} \tag{12.}$$

with $\mathbf{x} = \boldsymbol{\chi}(\mathbf{X}, t)$. In contrast, $\mathbf{t}$ is a force distribution that is similar to the Eulerian force density defined in Section 2.1 for the case of a thin interface. Here, $\mathbf{t}$ induces a discontinuity in the traction associated with the extended fluid stress, $\overline{\sigma}^{\mathrm{f}}$. In fact, traction continuity requires $[\![\sigma \mathbf{n}]\!] = \mathbf{0}$, but because we have $\overline{\sigma}^{\mathrm{s}} = \mathbf{0}$ in $\Omega_t^{\mathrm{f}}$ and $\sigma = \overline{\sigma}^{\mathrm{f}} + \overline{\sigma}^{\mathrm{s}}$, force balance requires $[\![\overline{\sigma}^{\mathrm{f}} \mathbf{n}]\!] = -\sigma^{\mathrm{s}} \mathbf{n}$ on $\Gamma_t^{\mathrm{fs}}$, in which $\sigma^{\mathrm{s}} \mathbf{n}$ is taken to be the limiting value of the solid traction as we approach $\Gamma_t^{\mathrm{fs}}$. This is precisely the discontinuity generated by $\mathbf{t}$ along $\Gamma_t^{\mathrm{fs}}$.

It is possible to obtain an equivalent formulation of Equations 5–9 that eliminates $\mathbf{t}$ and involves only a single volumetric Lagrangian force density by requiring $\mathbf{F}$ to satisfy

$$\int_{\Omega_0^{\mathrm{s}}} \mathbf{F}(\mathbf{X}, t) \cdot \mathbf{V}(\mathbf{X}) \, \mathrm{d}\mathbf{X} = -\int_{\Omega_0^{\mathrm{s}}} \mathbb{P}^{\mathrm{s}}(\mathbf{X}, t) : \nabla_{\mathbf{X}} \mathbf{V}(\mathbf{X}) \, \mathrm{d}\mathbf{X} \qquad 13.$$

for all smooth Lagrangian test functions $\mathbf{V}(\mathbf{X})$ (Boffi et al. 2008, Griffith & Luo 2017). As in the case of an immersed boundary, some numerical methods replace the singular delta function by a regularized delta function. The immersed finite-element method of Zhang et al. (2004) was the first numerical method developed for this formulation. It uses finite-element discretizations of both the Lagrangian and Eulerian domains. Boffi et al. (2008) introduced a variational formulation of these equations that avoids regularizing the delta function and that is naturally implemented using finite-element methods. This formulation yields improved accuracy as compared to regularized discretization schemes, but this method does not typically realize the optimal convergence rates of the underlying finite-element spaces (Boffi et al. 2008). Achieving higher-order accuracy appears to require a more direct treatment of the stress discontinuity along the interface. Methods have also been developed that retain finite-difference or finite-volume schemes for the Eulerian equations (Zhao et al. 2008, Devendran & Peksin 2012, Griffith & Luo 2017, Saadat et al. 2018).

**2.2.2. Elasticity models.** This volumetric formulation is well suited for structural models formulated using the framework of nonlinear continuum mechanics (Holzapfel 2000). We sketch only briefly the formulation of hyperelastic structural models, which are widely used to describe biological materials. These models describe the elastic material response by a (local) strain energy functional $\Psi(\mathbb{F})$ of the deformation gradient tensor $\mathbb{F} = \partial \boldsymbol{\chi} / \partial \mathbf{X}$. For such a material, the first Piola–Kirchhoff stress is $\mathbb{P}^{\mathrm{s}} = \partial \Psi / \partial \mathbb{F}$. To obtain an isotropic material model that is invariant under rigid-body motions, we formulate $\Psi$ using the principal invariants of an objective strain measure such as the right Cauchy–Green strain, $\mathbb{C} = \mathbb{F}^T \mathbb{F}$. Anisotropic material models can be defined similarly in terms of pseudo-invariants of $\mathbb{C}$.

In principle, the immersed formulations described herein ensure that the structure is exactly incompressible because we have $\nabla \cdot \mathbf{u} \equiv 0$ in $\Omega$ and $\frac{\partial \boldsymbol{\chi}}{\partial t}(\mathbf{X}, t) = \mathbf{u}[\boldsymbol{\chi}(\mathbf{X}, t), t]$. However, numerical methods for these formulations may allow for compressive or dilational motions, and it is useful to consider elasticity formulations for nearly incompressible large-deformation elasticity. In such formulations, it is common to postulate a decoupled volumetric response, $\Psi = W(\mathbb{F}) + U(J)$, in which $W(\mathbb{F})$ characterizes the response of the material to shearing deformations and $U(J)$ is a volumetric energy that penalizes compression or dilation. In this context, it is useful for $U$ to satisfy $U(1) = U'(1) = 0$, so that no additional energy or stress is associated with incompressible deformations. Choosing a penalty term of the form $U(J) = \frac{K}{2}(\ln J)^2$ yields the pressure $-K \ln J / J$, and $K$ can be related to the bulk modulus of the compressible material model. Because the immersed formulation implies $J \equiv 1$, however, $K$ is more clearly interpreted as a stabilization parameter in numerical methods for the equations of motion.

It can also be beneficial to formulate the shearing energy using modified invariants that are based on multiplicatively decomposing $\mathbb{F}$ into dilational and deviatoric parts, $\mathbb{F} = J^{\frac{1}{3}} \overline{\mathbb{F}}$. If we use

the invariants of $\overline{\mathbb{C}} = \overline{\mathbb{F}}^T \overline{\mathbb{F}}$ to define the shearing energy, $\overline{W} = W(\overline{\mathbb{F}})$, then the Cauchy stress, $\overline{\sigma}^s = J^{-1} \frac{\partial \overline{W}}{\partial \overline{\mathbb{F}}} \mathbb{F}^{-T}$, is traceless. Notice that by construction, $\det(\overline{\mathbb{F}})$ equals 1, and so energies that depend only on modified invariants are oblivious to volume changes.

### 2.3. Constrained Kinematics

When introducing deformational constraints on the motion of the structure, the Lagrangian force becomes a Lagrange multiplier for the kinematic constraint. The simplest case to consider is that of a body that moves with a prescribed velocity $\mathbf{V}(\mathbf{X}, t)$,

$$\rho \frac{\mathrm{D}\mathbf{u}}{\mathrm{D}t}(\mathbf{x}, t) = -\nabla p(\mathbf{x}, t) + \mu \nabla^2 \mathbf{u}(\mathbf{x}, t) + \int_{\Omega_0^s} \mathbf{F}(\mathbf{X}, t)\, \delta[\mathbf{x} - \boldsymbol{\chi}(\mathbf{X}, t)]\, \mathrm{d}\mathbf{x}, \tag{14.}$$

$$\nabla \cdot \mathbf{u}(\mathbf{x}, t) = 0, \tag{15.}$$

$$\mathbf{U}(\mathbf{X}, t) = \int_{\Omega} \mathbf{u}(\mathbf{x}, t)\, \delta[\mathbf{x} - \boldsymbol{\chi}(\mathbf{X}, t)]\, \mathrm{d}\mathbf{x}, \tag{16.}$$

$$\mathbf{U}(\mathbf{X}, t) = \mathbf{V}(\mathbf{X}, t), \tag{17.}$$

$$\frac{\partial \boldsymbol{\chi}}{\partial t}(\mathbf{X}, t) = \mathbf{V}(\mathbf{X}, t). \tag{18.}$$

This formulation can be extended to treat structures with prescribed deformational kinematics, including both rigid and deforming bodies (Glowinski et al. 1999, Patankar et al. 2000, Sharma & Patankar 2005, Apte et al. 2009, Shirgaonkar et al. 2009, Bhalla et al. 2013, Balboa Usabiaga et al. 2016, Kallemov et al. 2016, Nangia et al. 2017b).

Effective solution methods have been developed for the fully constrained formulation (Taira & Colonius 2007, Balboa Usabiaga et al. 2016, Kallemov et al. 2016), but in practice, it can suffice to use penalty formulations that relax the constraint. One approach uses frictional penalty forces. This formulation is identical to Equations 14–18, except that it does not require $\mathbf{U} \equiv \mathbf{V}$, and the Lagrangian force density is proportional to the velocity mismatch, $\mathbf{F}(\mathbf{X}, t) = \eta\, [\mathbf{V}(\mathbf{X}, t) - \mathbf{U}(\mathbf{X}, t)]$. In the limit $\eta \to \infty$, the Lagrangian representation of the Eulerian velocity, $\mathbf{U}(\mathbf{X}, t)$, approaches the motion prescribed by $\mathbf{V}(\mathbf{X}, t)$. These methods are particularly effective if shear stresses dominate the fluid forcing on the structure, as in external flow problems at moderate to high Reynolds numbers (*Re*).

An alternative approach introduces spring-like penalty forces, which can be more effective than frictional forces if the structure must support a substantial pressure load. In this approach, the deformation mapping $\boldsymbol{\chi}(\mathbf{X}, t)$ moves with the fluid, $\frac{\partial \boldsymbol{\chi}}{\partial t}(\mathbf{X}, t) = \mathbf{U}(\mathbf{X}, t)$, and an auxiliary mapping $\boldsymbol{\phi}(\mathbf{X}, t)$ moves according to the prescribed velocity field, $\frac{\partial \boldsymbol{\phi}}{\partial t}(\mathbf{X}, t) = \mathbf{V}(\mathbf{X}, t)$. A Lagrangian force density acts to keep these two configurations together, $\mathbf{F}(\mathbf{X}, t) = \kappa\, (\boldsymbol{\phi}(\mathbf{X}, t) - \boldsymbol{\chi}(\mathbf{X}, t))$. In the limit $\kappa \to \infty$, the deformation mapping that moves with the Eulerian velocity, $\boldsymbol{\chi}(\mathbf{X}, t)$, approaches the motion prescribed by $\boldsymbol{\phi}(\mathbf{X}, t)$, and the penalty method recovers the exactly constrained formulation. In practice, combining frictional and spring-like forces can limit spurious oscillations.

## 3. NUMERICAL METHODS

### 3.1. Eulerian Spatial Discretization

Although many different Eulerian discretizations may be used, for concreteness, consider $\Omega = [0, L]^3$ and introduce a uniform $N \times N \times N$ Cartesian grid on $\Omega$ with grid spacing $h = L/N$. Let

$(i, j, k)$ index the Cartesian grid cells, $0 \leq i, j, k < N$, with $\mathbf{x}_{i,j,k} = \left((i + \frac{1}{2})h, (j + \frac{1}{2})h, (k + \frac{1}{2})h\right)$. The pressure is approximated at the cell centers, and the normal components of $\mathbf{u} = (u_1, u_2, u_3)$ are approximated on the grid cell faces, so that component $u_g$ $(g = 1, 2, 3)$ is approximated at position $\mathbf{x}_{i+\alpha_{1g}, j+\alpha_{2g}, k+\alpha_{3g}} = \left((i + \frac{1}{2} + \alpha_{1g})h, (j + \frac{1}{2} + \alpha_{2g})h, (k + \frac{1}{2} + \alpha_{3g})h\right)$, with $\alpha_{ij} = -\frac{\delta_{ij}}{2}$ and $\delta_{ij}$ the Kronecker delta. Eulerian forces, including the pressure gradient, are also approximated on the cell faces. We use staggered second-order approximations to $\nabla \cdot \mathbf{u}$ at the cell centers, denoted $\mathbf{D} \cdot \mathbf{u}$, and to $\nabla p$ on the grid faces, denoted $\mathbf{G}p$, for which we have $\mathbf{D} \cdot = -\mathbf{G}^T$ and $L = \mathbf{D} \cdot \mathbf{G}$ is the seven-point Laplacian (Griffith 2009). We use shifted versions of the scalar Laplacian to approximate the viscous term on the grid faces, $\mu \mathbf{L}\mathbf{u} = \mu\,(Lu_1, Lu_2, Lu_3)$. These approximations can be extended to locally refined grids (Griffith 2012, Griffith & Lim 2012).

An effective approach to approximating $\mathbf{u} \cdot \nabla \mathbf{u}$ is to construct control volumes centered about the velocity components and to apply a high-resolution convective discretization (Colella & Sekora 2008, Nonaka et al. 2011, Ketcheson et al. 2013) on each control volume (Griffith 2009). It also is possible to construct centered approximations to the convective term on staggered grids (Morinishi et al. 1998). Such schemes can be used across a very broad range of flow regimes (Morinishi et al. 1998, Balboa Usabiaga et al. 2012).

## 3.2. Lagrangian Spatial Discretizations

This section briefly describes structural discretizations commonly used with these formulations.

**3.2.1. Marker points.** A simple Lagrangian spatial discretization is to describe the structure using a collection of marker points that move according to the interpolated Eulerian velocity field. These descriptions are well suited for the fiber-based elasticity model outlined in Section 2.1.3. We use $l$ to label individual Lagrangian markers and staggered differences to approximate $T$ and $\boldsymbol{\tau}$. For a Hookean spring model with zero resting length, we have $\mathbf{F}_l = \frac{S}{\Delta q^2}\left(\boldsymbol{\chi}_{l-1} - 2\boldsymbol{\chi}_l + \boldsymbol{\chi}_{l+1}\right)$. Nonlinear length–tension relationships can also be used.

**3.2.2. Finite-element meshes.** If $\{\phi_l(\mathbf{x})\}$ are nodal finite-element basis functions associated with a triangulation of $\Omega_0^s$, we can construct a continuous representation of the structural deformation and force via $\boldsymbol{\chi}(\mathbf{X}, t) = \sum_l \boldsymbol{\chi}_l(t)\,\phi_l(\mathbf{x})$ and $\mathbf{F}(\mathbf{X}, t) = \sum_l \mathbf{F}_l(t)\,\phi_l(\mathbf{x})$, in which $\boldsymbol{\chi}_l$ and $\mathbf{F}_l$ are nodal deformations and forces, respectively. Using these representations with Equation 13 and restricting the test functions to the finite-element basis functions leads to a standard Galerkin finite-element method for the structural mechanics model. This approach has been used in various versions of the immersed finite-element method. One strength of this formulation is that the discrete representations of $\boldsymbol{\chi}(\mathbf{X}, t)$ and $\mathbf{F}(\mathbf{X}, t)$ can be evaluated anywhere on the triangulation of $\Omega_0^s$ and not only at the nodes. Marker point-based descriptions of the structure can be viewed as special cases in which discrete approximations to $\boldsymbol{\chi}(\mathbf{X}, t)$ and $\mathbf{F}(\mathbf{X}, t)$ are evaluated only at the nodes of the finite-element mesh.

## 3.3. Lagrangian–Eulerian Interaction

This section briefly details numerical strategies for coupling the Lagrangian and Eulerian variables.

**3.3.1. Regularized delta functions.** On a uniform Cartesian grid, it is natural to construct the three-dimensional delta function as the tensor product of one-dimensional delta functions and to

relate the regularization parameter to the grid spacing $h$, so that the regularized delta function is $\delta_h(\mathbf{x}) = \prod_{i=1}^{3} \delta_h(x_i)$, with $\delta_h(x) = \frac{1}{h}\varphi\left(\frac{x}{h}\right)$. If a nodal quadrature rule with quadrature weights $\Delta\mathbf{q}_l$ is used to approximate a regularized version of Equation 3, the discretized Eulerian and Lagrangian forces are related by

$$\left(f_g\right)_{i+\alpha_{1g},j+\alpha_{2g},k+\alpha_{3g}} = \sum_l \left(F_g\right)_l \, \delta_h\left(\mathbf{x}_{i+\alpha_{1g},j+\alpha_{2g},k+\alpha_{3g}} - \boldsymbol{\chi}_l\right) \Delta\mathbf{q}_l, \; g = 1,2,3, \tag{19.}$$

with $\mathbf{f} = (f_1, f_2, f_3)$ and $\mathbf{F} = (F_1, F_2, F_3)$. As above, we use $\alpha_{ij} = -\frac{\delta_{ij}}{2}$ and $\delta_{ij}$ is the Kronecker delta. More compactly, we have $\mathbf{f} = \boldsymbol{\mathcal{S}}_{\text{IB}}[\boldsymbol{\chi}]\,\mathbf{F}$, in which $\boldsymbol{\mathcal{S}}_{\text{IB}}$ is the force-spreading operator. Lagrangian and Eulerian velocities can be related by a similar discretization of Equation 4,

$$\left(U_g\right)_l = \sum_{i,j,k} \left(u_g\right)_{i+\alpha_{1g},j+\alpha_{2g},k+\alpha_{3g}} \, \delta_h\left(\mathbf{x}_{i+\alpha_{1g},j+\alpha_{2g},k+\alpha_{3g}} - \boldsymbol{\chi}_l\right) h^3, \; g = 1,2,3, \tag{20.}$$

with $\mathbf{U} = (U_1, U_2, U_3)$ and $\mathbf{u} = (u_1, u_2, u_3)$. We write $\mathbf{U} = \boldsymbol{\mathcal{J}}_{\text{IB}}[\boldsymbol{\chi}]\,\mathbf{u}$, in which $\boldsymbol{\mathcal{J}}_{\text{IB}}$ is the velocity interpolation operator. In this construction, the spreading and interpolation operators are discretely adjoint with respect to discrete Eulerian and Lagrangian inner products induced by the quadrature rules. If the Lagrangian quadrature weights are uniform, so that $\Delta\mathbf{q}_l \equiv \Delta\mathbf{q}$, then the force-spreading operator and the velocity-interpolation operators satisfy the relation $\boldsymbol{\mathcal{J}}_{\text{IB}} = \frac{h^3}{\Delta\mathbf{q}}\boldsymbol{\mathcal{S}}_{\text{IB}}^T$. More generally, we have $\boldsymbol{\mathcal{J}}_{\text{IB}} = \boldsymbol{\mathcal{S}}_{\text{IB}}^* = h^3\,\boldsymbol{\mathcal{M}}^{-1}\,\boldsymbol{\mathcal{S}}_{\text{IB}}^T$, in which $\boldsymbol{\mathcal{M}}$ is a diagonal mass matrix with $M_{ll} = \Delta\mathbf{q}_l$.

If $\boldsymbol{\chi}$ and $\mathbf{F}$ can be evaluated at arbitrary material positions, and not just at the marker points or nodes, it is possible to use other quadrature rules to approximate the interaction equations. For instance, Griffith & Luo (2017) developed an adjoint pair of coupling operators for finite-element structural models that use Gaussian quadrature to approximate these integrals. With nodal quadrature rules, if the Lagrangian nodes or marker points become too far apart with respect to the background grid, the structure will develop leaks (Peskin 2002). Using non-nodal quadrature rules permits the structural discretization to be relatively coarse compared to the background Cartesian grid without allowing fluid to leak through the structural discretization so long as the net of quadrature points is sufficiently dense (Griffith & Luo 2017).

It remains to specify the basic kernel function, $\varphi(r)$. Computational considerations motivate choices of $\varphi(r)$ with the minimum support that provide a required level of accuracy. A fundamental accuracy requirement is that $\varphi(r)$ ensures that the Eulerian and Lagrangian expressions for the total force and total torque agree, so that the coupling scheme does not induce spurious rigid-body motions. As detailed by Peskin (2002), these identities follow from imposing two discrete moment conditions on $\varphi(r)$, $\sum_j \varphi(r-j) = 1$ and $\sum_j (r-j)\,\varphi(r-j) = 0$ for all $r \in \mathbb{R}$. These conditions imply that $\boldsymbol{\mathcal{J}}_{\text{IB}}$ interpolates linear fields exactly, which yields an interpolation error of $\mathcal{O}(h^2)$ for smooth fields. Peskin's construction also imposes an approximate translation invariance property, $\sum_j \left[\varphi(r-j)\right]^2 = C$ for all $r \in \mathbb{R}$. It is possible to impose higher-order discrete moment conditions, which yield improved interpolation accuracy for smooth fields but generate kernels that do not satisfy $\varphi \geq 0$. Bao et al. (2016) introduced an alternative construction that imposes a constant, but nonzero, second moment condition along with a standard third moment condition, and they showed that it is possible to choose the second moment condition so that $\varphi$ is non-negative and has three continuous derivatives.

One alternative approach is to use B-spline kernels (**Figure 2**), which is effective at moderate-to-high Reynolds numbers, including the cardiovascular modeling application shown in Section 5.3.1 in which the Reynolds number reaches approximately 20,000. We define $B_0(r)$ to be

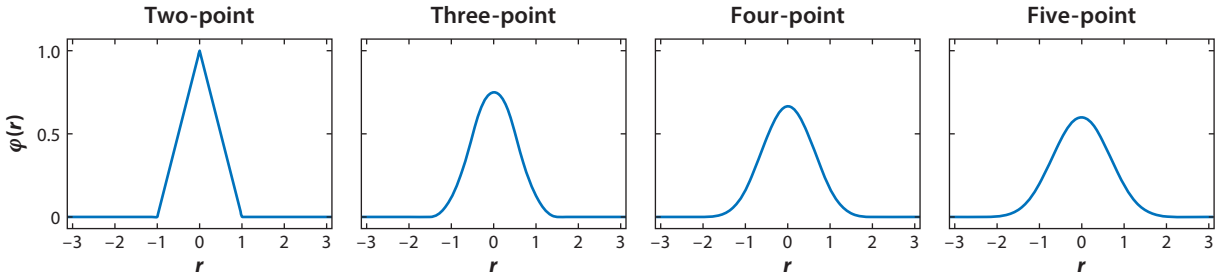


**Figure 2**

Two-, three-, four-, and five-point B-spline kernel functions. The limiting function is a Gaussian. A one-dimensional regularized delta function $\delta_h(x)$ may be defined in terms of a basic kernel function $\varphi(r)$ via $\delta_h(x) = \frac{1}{h}\varphi(\frac{x}{h})$. The three-dimensional regularized delta function $\delta_h(\mathbf{x})$ can then be obtained by $\delta_h(\mathbf{x}) = \delta_h(x)\delta_h(y)\delta_h(z)$.

the lowest-order B-spline kernel,

$$B_0(r) = \begin{cases} 1, & \text{if } |r| \leq \frac{1}{2}, \\ 0, & \text{otherwise.} \end{cases} \tag{21.}$$

The $k$-th-order B-spline kernel is built recursively via convolution, $B_k = B_{k-1} * B_0$. $B_k$ is a $C^{k-1}$-continuous piecewise polynomial function with a support of $k+1$ mesh widths.

On nonuniform grids, alternative methods are required to construct regularized delta functions. For instance, the immersed finite-element method of Zhang et al. (2004) uses regularized kernel functions that are determined by the reproducing particle kernel method (Liu et al. 1995), which ensures that the interpolation operator is able to reproduce certain fields exactly. These conditions can be seen to be generalizations of the discrete moment conditions that are readily used with regular Cartesian grids.

**3.3.2. Jump conditions.** It is possible to build discontinuities directly into finite-difference approximations (Xu & Wang 2006b). Briefly, if $u(x)$ has a known collection of discontinuities at $x^\star \in [x_i, x_{i+1}]$, then a generalized Taylor analysis yields

$$\frac{\mathrm{d}u}{\mathrm{d}x}\left(x_{i+\frac{1}{2}}\right) = \frac{u_{i+1} - u_i}{h} - \frac{1}{h}\sum_{m=0}^{2} \frac{r^m}{m!}\left[\!\left[\frac{\mathrm{d}^m u}{\mathrm{d}x^m}(x^\star)\right]\!\right] + \mathcal{O}(h^2), \tag{22.}$$

with $r = \min(x^\star - x_i, x_{i+1} - x^\star)$. If the jump conditions are independent of $u$, this expression splits into a standard finite-difference approximation and an inhomogeneous term that can be treated as a forcing. Similar expressions can be developed for higher-order derivatives.

For the immersed interface formulation described here, the jump conditions depend only on $\mathbf{F}(\mathbf{q}, t)$ and the configuration of the interface, and so at the level of the discrete equations, we can account for the jump conditions through a discrete force spreading operator, $\mathbf{f} = \mathcal{S}_{\text{IIM}}[\chi]\ \mathbf{F}$, that is tailored to the finite-difference approximations used in solving the incompressible Navier–Stokes equations. It is possible to build a velocity interpolation operator $\mathcal{J}_{\text{IIM}}$ that accounts for the known discontinuities in the derivatives of $\mathbf{u}$. Unlike the immersed boundary method, however, generally $\mathcal{J}_{\text{IIM}}$ is not $\mathcal{S}^*_{\text{IIM}}$.

### 3.4. Time Stepping

For dynamic simulations involving immersed elastic structures, it often suffices to employ explicit coupling between the fluid and the structure. We index the time step by $n$ and for simplicity assume a uniform time step size $\Delta t$, so that $t^n$ corresponds to the time $n\Delta t$. A prototypical second-order accurate time stepping scheme takes the form

$$\rho\left(\frac{\mathbf{u}^{n+1}-\mathbf{u}^n}{\Delta t}+\mathbf{N}^{n+\frac{1}{2}}\right)=-\mathbf{G}p^{n+\frac{1}{2}}+\mu\mathbf{L}\left(\frac{\mathbf{u}^{n+1}+\mathbf{u}^n}{2}\right)+\mathcal{S}\left[\chi^{n+\frac{1}{2}}\right]\mathbf{F}\left[\chi^{n+\frac{1}{2}}\right], \tag{23.}$$

$$\mathbf{D}\cdot\mathbf{u}^{n+1}=0, \tag{24.}$$

$$\frac{\chi^{n+\frac{1}{2}}-\chi^n}{\Delta t/2}=\mathcal{J}[\chi^n]\,\mathbf{u}^n, \tag{25.}$$

$$\frac{\chi^{n+1}-\chi^n}{\Delta t}=\mathcal{J}\left[\chi^{n+\frac{1}{2}}\right]\left(\frac{\mathbf{u}^{n+1}+\mathbf{u}^n}{2}\right), \tag{26.}$$

in which $\mathbf{N}^{n+\frac{1}{2}}$ is an explicit, time step–centered approximation to $\mathbf{u}\cdot\nabla\mathbf{u}$. Using an explicit scheme for the convective term imposes a stability constraint on the largest stable time step size, but that constraint is usually less severe than the constraint imposed by treating the coupling between the Eulerian and the Lagrangian variables explicitly in time. Newren et al. (2007) determined sufficient conditions to obtain a linearly stable implicit time-stepping scheme, but explicit coupling schemes remain widely used in large-scale simulations because efficient general-purpose implicit solver algorithms are still lacking.

The penalty methods described in Section 2.3 introduce force models that approximately impose kinematic constraints, and such formulations can be accommodated by this time-stepping scheme. Effective methods for constrained problems also can be developed through physical considerations. An example is the time step–splitting scheme of Bhalla et al. (2013) for immersed structures with prescribed deformational kinematics. The success of splitting methods like that of Bhalla et al. (2013) fundamentally relies on the presence of inertia. Such methods can break down in the overdamped limit, and it then becomes necessary to use a fully implicit formulation (Balboa Usabiaga et al. 2016, Kallemov et al. 2016).

## 4. BENCHMARK PROBLEMS

### 4.1. External Flows

The benchmark problem of viscous flow passing over a stationary cylinder has been very widely studied in the literature, including by Lai & Peskin (2000) and Taira & Colonius (2007). We used the domain geometry and boundary conditions specified by Taira & Colonius (2007) along with a spring-based penalty method and achieved lift and drag coefficients and Strouhal numbers that are in agreement with the results reported therein (Griffith & Luo 2017, Kolahdouz et al. 2019). **Figure 3** compares immersed boundary and immersed interface simulations of this problem at $Re = 200$. Both formulations reproduce the large-scale flow features of the wake, but the immersed boundary formulation generates spurious interior fluid motion that is eliminated in the immersed interface calculation. The reason for this difference is that the immersed boundary method determines the motion of the interface through a local averaging operation, and so an exterior flow along the boundary will tend to generate a counter-rotating interior flow. In

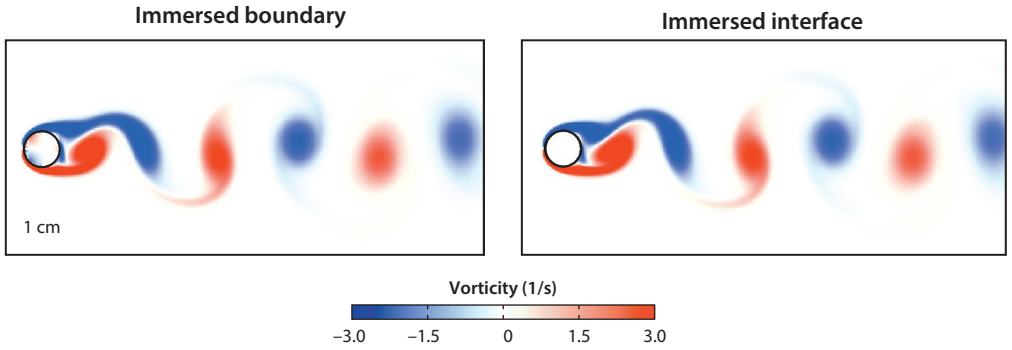


**Figure 3**

Vorticity fields for viscous flow over a circular cylinder at Reynolds number $Re = 200$ by immersed boundary (*left*) and immersed interface (*right*) methods. Both methods produce essentially identical large-scale flow features in the wake behind the cylinder, but the immersed boundary formulation generates spurious interior motion that is eliminated in the immersed interface calculation.

contrast, the immersed interface method is able to reconstruct the discontinuity in the derivative of the velocity that occurs along the interface.

### 4.2. Large-Deformation Incompressible Elasticity

Benchmarking studies reported by Wang & Zhang (2010) demonstrated poor volume conservation by the immersed finite-element method (Zhang et al. 2004), and although they proposed a volume-correction scheme to mitigate these errors, this scheme is ad hoc and somewhat expensive to use in practice. These difficulties were largely resolved by Vadala-Roth et al. (2018), who considered the performance of a similar method in the context of several standard test cases from the nonlinear mechanics literature. Their key finding was that immersed methods can realize an accuracy comparable to that provided by stabilized finite-element methods for incompressible nonlinear elasticity by adopting a nearly incompressible elasticity formulation like that detailed in Section 2.2.2. In particular, the accuracy of the immersed formulation is improved dramatically for invariant-based elasticity formulations by using both a volumetric penalization term, which we view as a stabilization method, and invariants based on the modified deformation gradient tensor, $\overline{\mathbb{F}} = J^{-\frac{1}{3}}\mathbb{F}$. **Figure 4** shows results from a torsion test, similar to one by Bonet et al. (2015), that demonstrates the effectiveness of the methodology.

## 5. APPLICATIONS

### 5.1. Aquatic Locomotion

Immersed methods are well suited for the study of aquatic locomotion (i.e., swimming), and this section outlines examples of studies enabled by these methods.

There is a longstanding interest in understanding what role hydrodynamics may have played in the evolution of fish form (Webb 1984), and this same understanding can also help in designing underwater vehicles (MacIver et al. 2004). Immersed methods have been especially successful in studies of optimal conditions for swimming at finite Reynolds number. Examples include investigations of optimal deformation kinematics (Kern & Koumoutsakos 2006; Borazjani & Sotiropoulos 2008, 2009; Shirgaonkar et al. 2008; Gazzola et al. 2012; Bale et al. 2015; Nangia

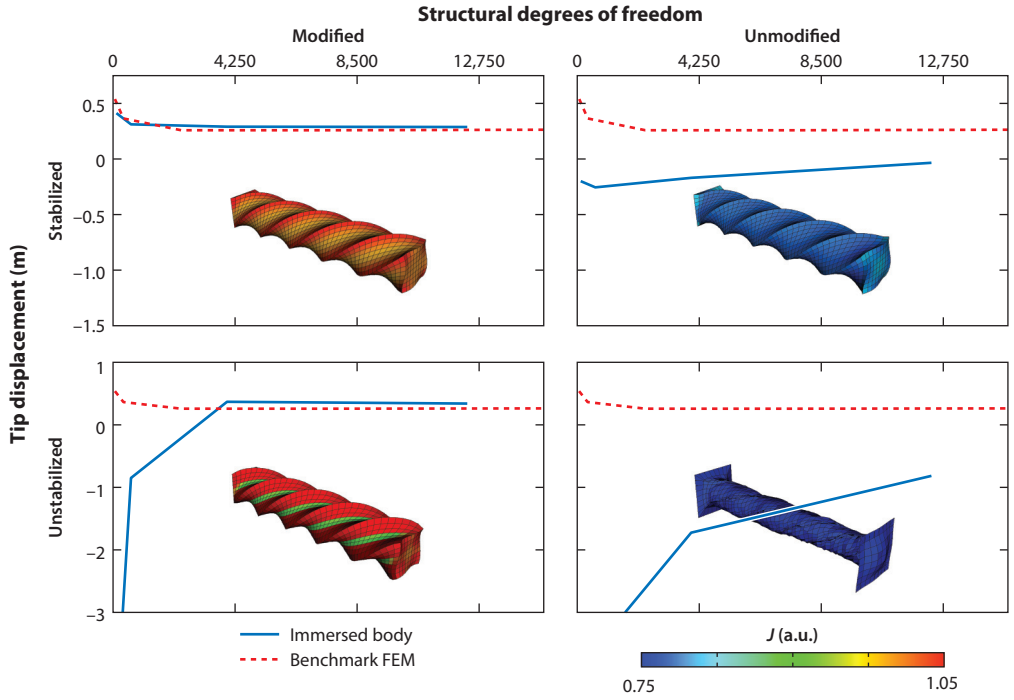


**Figure 4**

Torsion test demonstrating the effect of the form of the elasticity model on the accuracy of the immersed finite-element method (FEM). The face of an incompressible elastic beam with a Mooney–Rivlin material model is twisted 450°. Four elasticity formulations are considered. "Stabilized" indicates that a volumetric energy, $U(J)$, is included in the strain energy $\Psi$; "unstabilized" indicates that this energy is not included in $\Psi$. "Unmodified" indicates that the shearing energy $W$ is expressed in terms of the invariants of the right Cauchy–Green tensor, $\mathbb{C} = \mathbb{F}^T\mathbb{F}$, in which $\mathbb{F}$ is the deformation gradient tensor; "modified" indicates that the invariants of the modified Cauchy–Green strain $\overline{\mathbb{C}} = \overline{\mathbb{F}}^T\overline{\mathbb{F}}$ are used, with $\overline{\mathbb{F}} = J^{-\frac{1}{3}}\mathbb{F}$. The immersed formulation yields an accuracy comparable to benchmark FEM results when using both modified invariants and volumetric stabilization.

et al. 2017a; Sprinkle et al. 2017b), body shapes (van Rees et al. 2013), and swimming configurations (Verma et al. 2018). Swimming and flying animals have been reported to cruise at Strouhal numbers of 0.2–0.4 (Taylor et al. 2003). A related optimality condition has been discovered from simulations and experiments for undulatory swimming: A wavelength-to-mean amplitude ratio of 20 maximizes the speed (or thrust) in undulatory propulsion (Bale et al. 2015, Nangia et al. 2017a). This optimality condition appears to have convergently evolved at least eight times in elongated fin swimmers (Bale et al. 2015).

Immersed simulations have provided insight into long-debated issues, including the separation of drag and thrust on swimming bodies (Bale et al. 2014c), Gray's paradox (Bale et al. 2014b), and energy efficiency (Bale et al. 2014a). The standard conceptual framework seeks to understand swimming as a balance between drag and thrust, but it is not obvious how to arrive at such a separation for undulatory swimmers because their drag- and thrust-producing regions are not distinct. Nonetheless, such a separation is possible under certain conditions (Bale et al. 2014c). Remarkably, this particular drag–thrust separation framework helps to predict the observed height of the ribbon fin of the electric knifefish, which is an important model system for highly maneuverable underwater vehicles. Similar simulations also reveal questions about the common assumption that swimmers necessarily spend muscle energy to overcome drag in the direction

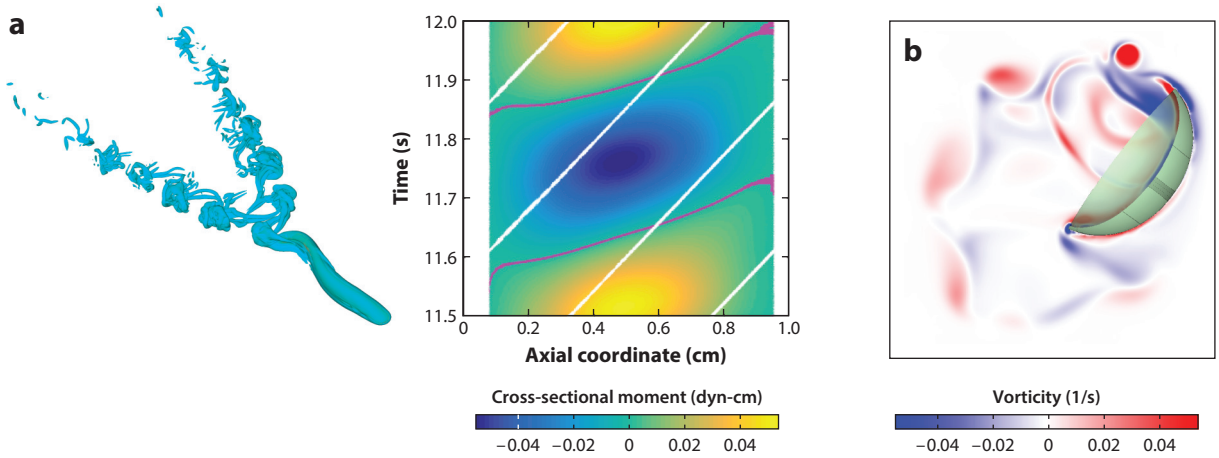


**Figure 5**

(*a*) Three-dimensional simulation of neurally activated swimming eel using a constraint-based immersed method (Patel et al. 2018). (*Left*) Fluid vorticity field; (*right*) color contour of the cross-sectional moment of the body. Magenta lines and white lines show the progression of the moment wave and the curvature wave, respectively. The difference in slopes of the two lines is the neuromechanical phase lag consistent with experimental observations. Panel adapted with permission from Patel et al. (2018). (*b*) Immersed simulation of jellyfish turning using a hyperelastic structural model similar to those of Hoover et al. (2017, 2019).

of swimming. For example, in undulatory swimming, most of the muscle energy is expended to produce lateral undulations of the body. Drag power is balanced by thrust power, not by muscle power. In fact, depending on the drag model utilized, the drag power may be greater than muscle power, which would otherwise be considered paradoxical [as in Gray's paradox (Bale et al. 2014b)]. Finally, simulations have also provided insights into defining the efficiency of self-propelled bodies. Because all of the energy expended by swimming animals is eventually dissipated in the fluid, an appropriate efficiency measure is not obvious. One approach is to define an energy-consumption coefficient, which is a nondimensional measure of fuel consumption (Bale et al. 2014a). This measure is analogous to the concept of the drag coefficient.

The fluid dynamics of swimming is also important in developing neuromechanical models to understand the complex interactions between neuronal, sensory, muscular, and mechanical components of locomotor systems (Pearson et al. 2006). Neuromechanical models take as input the muscle activation pattern and solve for the motion of the swimming body and fluid. Two-dimensional (Tytell et al. 2010) and three-dimensional (Patel et al. 2018) models (**Figure 5*a***) have been reported. These simulations can help to understand control strategies for swimmers, as well as biologically observed phenomena such as the neuromechanical phase lag (Patel et al. 2018). Hoover et al. (2017, 2019) have developed similar models of jellyfish swimming using hyperelastic models of the jellyfish bell (**Figure 5*b***).

## 5.2. Esophageal Transport

Esophageal transport is a mechanical and physiological process that transfers the ingested food bolus from the pharynx to the stomach through the multilayered esophageal tube. This process involves interactions between the bolus; the esophageal wall, which is composed of mucosal, circular muscle (CM), and longitudinal muscle (LM) layers; and the neurally coordinated muscle activation, including CM contraction and LM shortening (Pouderoux et al. 1997, Nicosia & Brasseur 2002, Ghosh et al. 2005, Mittal et al. 2006). According to Cook (2008), 5–8% of the

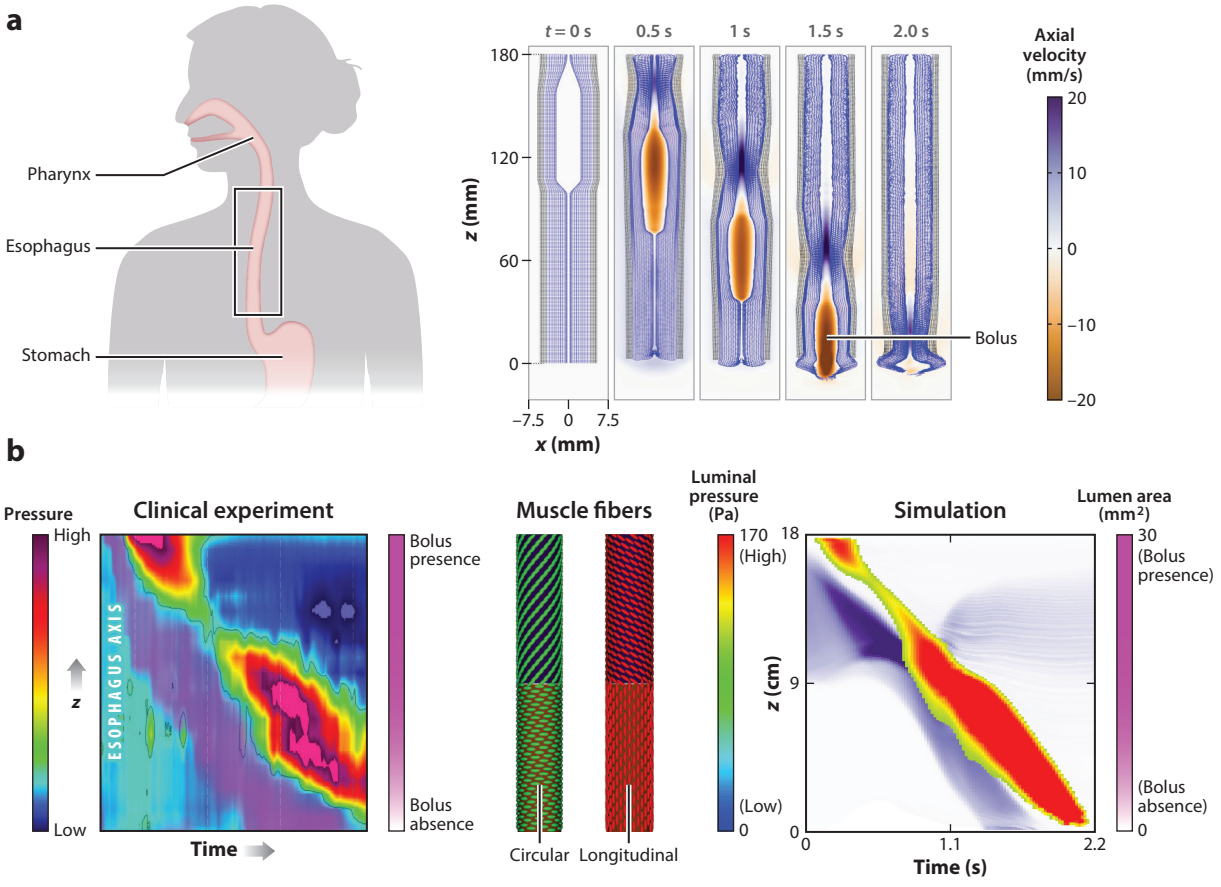


**Figure 6**

(*a*) Immersed simulation of bolus transport in an esophagus (Kou et al. 2015b). The brown region is the downward-moving bolus, and the blue and gray meshes represent the muscle layers. (*b*) Experimental (*left*) and simulated (*right*) esophageal pressure topography (EPT) of a normal subject. The fiber architecture, showing circular (*green*) and longitudinal (*red*) muscles that transition from proximal to distal ends, is shown in the center. Kou et al. (2017a) showed that the change in fiber architecture can lead to the well-known pressure transition zone in a normal patient. Panels adapted with permission from (*a*) Kou et al. (2015b) and (*b*) Kou et al. (2017a).

general population over 50 years of age exhibit symptoms of esophageal dysphagia (i.e., difficulty swallowing). Dysphagia is observed in 16% of the elderly and is common in chronic care settings (Cook 2008). It is a symptom of esophageal cancer, which is diagnosed in over 500,000 patients each year worldwide (Wheeler & Reed 2012). Dysphagia originates from mechanical abnormalities (e.g., of the muscles and mucosa) or neuromuscular disorders (i.e., abnormal muscle activation) (Castell & Donner 1987).

Simulating esophageal transport is challenging because it involves highly disparate length scales, from 0.3 mm to around 200 mm as the esophagus expands and contracts. It also involves very large deformations that result from interactions between the bolus and the esophagus. Kou et al. (2015a,b, 2017a,b, 2018) developed immersed models of esophageal transport in which the bolus is treated as a viscous fluid that is actively transported by the muscular esophagus, and the esophagus is modeled as an actively contracting, fiber-reinforced tube. **Figure 6*a*** shows a case from Kou et al. (2015a). Such models have enhanced our understanding of the roles of CM

contraction and LM shortening in esophageal transport. For instance, Kou et al. (2015b) found that CM contraction is sufficient to transport the bolus, but LM shortening is not.

Immersed models can also capture experimental observations, such as the manometric pressure transition zone in the esophagus shown in **Figure 6*b*** (Kou et al. 2017a). This information helps to relate clinical data from manometry to the underlying esophageal function. Ultimately, we envision translating these simulations into a clinical tool to inform diagnostic protocols of esophageal motility disorders, quantify disease pathogenesis, and plan treatment strategies. The models developed by Kou et al. (2015a,b, 2017a,b, 2018) are also directly applicable to medical device design. One set of devices can be used to assess the function and efficiency of the organ, loosely considered as diagnostic devices, and another set of devices can serve to restore lost function and provide structural support for weak tissue (e.g., stents). These models could also serve as the foundation for the development of a bioengineered esophagus for patients that undergo esophagectomy.

## 5.3. Cardiovascular Dynamics

The immersed boundary method was introduced by Peskin to model the fluid dynamics of heart valves. This section highlights recent applications of these methods to modeling cardiovascular dynamics.

**5.3.1. Bioprosthetic heart valves.** Computer models must be rigorously verified and validated before they can be used to design, optimize, or test medical devices or to customize patient treatment strategies. There has been substantial prior work on simulating heart valves, but nearly all validated valve models consider mechanical heart valves (MHVs) (Votta et al. 2013), including studies of bileaflet MHVs using high-speed cinematography (Nobili et al. 2008) and particle image velocimetry (Dasi et al. 2007, Ge et al. 2008, Guivier-Curien et al. 2009, Jun et al. 2014). Fewer studies have validated models of flexible valves such as bioprosthetic heart valves (BHVs). Quaini et al. (2012) validated a simplified elastic aperture model of a flexible heart valve using Doppler ultrasound. Wu et al. (2016) compared leaflet kinematics and valve open areas for an in vitro model of a transcatheter aortic valve replacement device, but did not provide detailed comparisons for hemodynamic parameters (pressures and flow rates) or comparisons to detailed flow patterns. Other recent work on fluid–structure interaction models of BHVs includes important aspects of validation (Hsu et al. 2015, Siguenza et al. 2018, Tango et al. 2018, Wu et al. 2018, Xu et al. 2018), but few of these studies use simulated flow conditions that are directly comparable to a corresponding experimental system, which is an important step toward validating such models.

Lee et al. (2019) developed immersed models of porcine tissue and bovine pericardial BHVs and simulated their performance in a model of a pulse duplicator, which is an in vitro experimental system for studying heart valve performance. The valve leaflets were described as fiber-reinforced hyperelastic structures, and the rigid wall of the pulse duplicator was described using a spring-based penalty method. **Figure 7** shows results obtained using the porcine tissue valve. Comparisons to experimental flow measurements are excellent, and the simulated and experimental leaflet kinematics are shown to be in good agreement. This study represents a necessary step toward the validation of immersed models of BHV dynamics.

**5.3.2. Inferior vena cava flows.** The inferior vena cava (IVC) returns deoxygenated blood to the heart from the lower extremities. Simulations of IVC flows are needed to study medical devices such as IVC filters, which are used in some patients with deep vein thrombosis who are at risk of

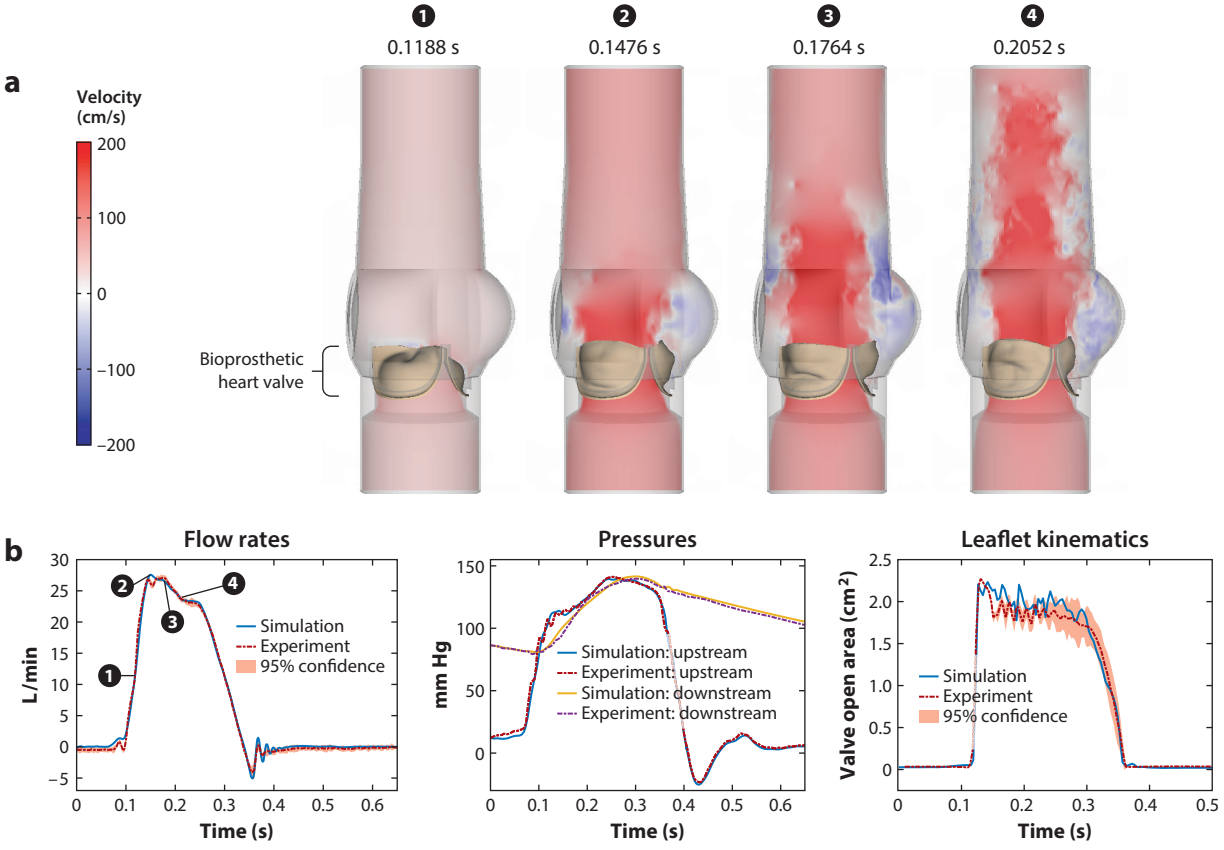


**Figure 7**

Model of a porcine bioprosthetic heart valve in an experimental pulse duplicator (Lee et al. 2019). (*a*) Simulated axial flow in the aortic test section. (*b*) Comparison of computational and experimental flow rates, upstream and downstream pressures, and leaflet kinematics quantified by valve open area. Shaded regions show the 95% confidence intervals in multicycle experimental data. Confidence intervals for the pressure data are extremely narrow and are not shown in panel *b*.

developing a pulmonary embolism but are unable to tolerate anticoagulation therapy. **Figure 8** shows initial comparisons between an immersed interface simulation of an idealized IVC model and corresponding simulations performed using a body-conforming discretization (Craven et al. 2018, Kolahdouz et al. 2019). The immersed interface simulation resolves the swirling flow patterns captured by the body-conforming method. Extensions of these models can be used to simulate clot-trapping IVC filters in studies that aim to improve our understanding of the safety and efficacy of these devices.

**5.3.3. Fluid–structure interaction models of the heart.** Since its inception, a major impetus to develop the immersed boundary method has been to enable simulations of cardiac dynamics (McQueen & Peskin 1989, 2000, 2001; Peskin & McQueen 1989, 1996). **Figure 9** shows results from two different immersed approaches to simulating cardiac dynamics. One, developed by Peskin, McQueen, and cowokers, uses a fiber-based construction of a patient-specific heart failure model (McQueen et al. 2015). The other, currently being developed by Griffith and coworkers, uses a finite-element description of the biomechanics of the heart, its valves, and the nearby

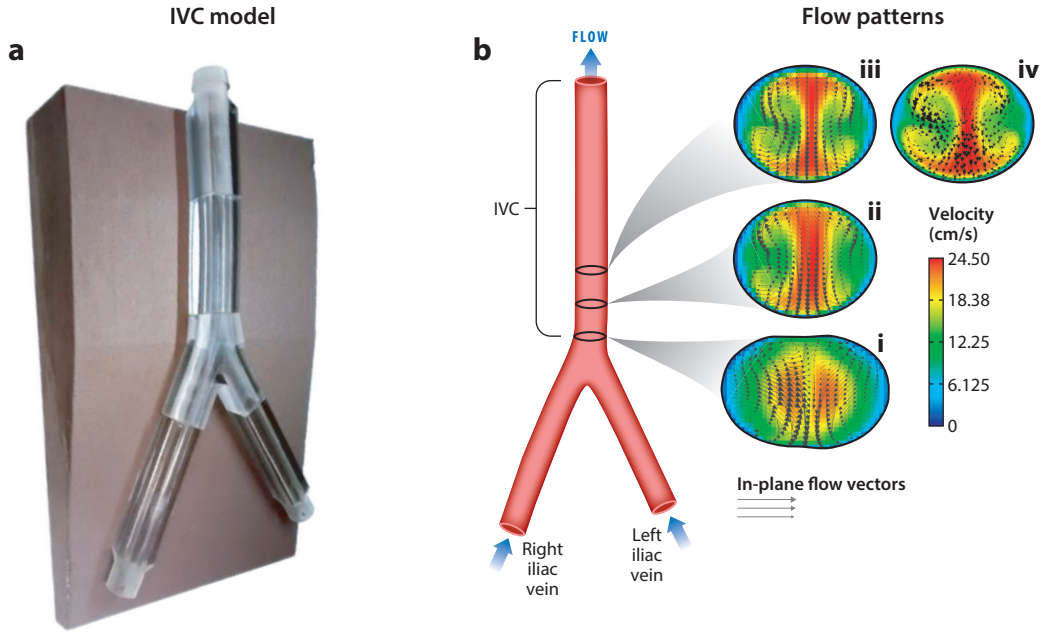


**Figure 8**

(*a*) Idealized inferior vena cava (IVC) model developed at the US Food and Drug Administration. (*b*) Simulation of flow in the idealized IVC model under exercise conditions (Kolahdouz et al. 2019). Subpanels *i–iv* show flow patterns along the cross-sections indicated on the three-dimensional model. Results were obtained using an immersed interface method (subpanels *i–iii*) and by a body-conforming method in OpenFOAM (subpanel *iv*) (Craven et al. 2018).

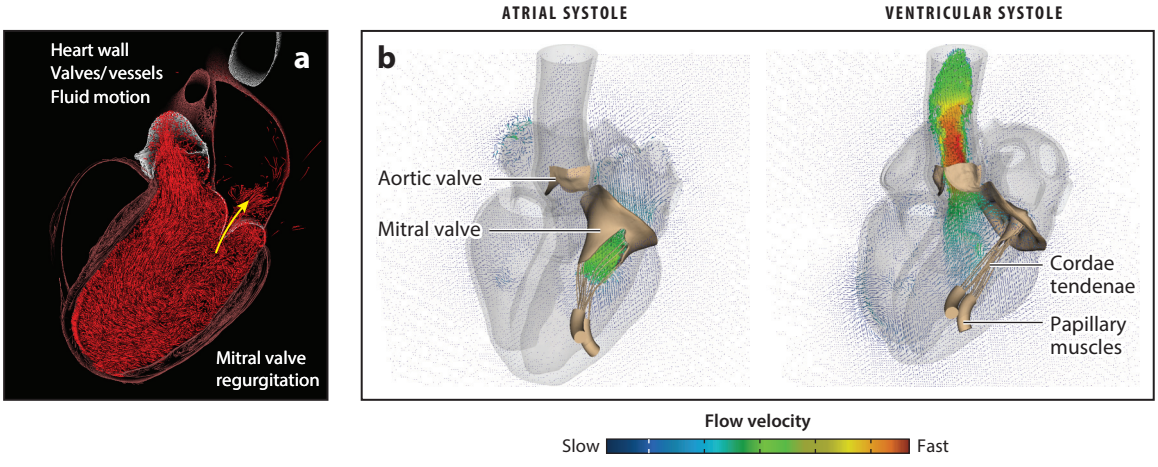


**Figure 9**

Fluid–structure interaction models of whole-heart dynamics. (*a*) Patient-specific fiber-based model of a failing heart in systole. Note mitral regurgitation has developed after several computed cardiac cycles during which the left ventricle enlarges slightly on each beat because more blood is returning to it than can be pumped away. (*b*) A healthy heart model that uses hyperelastic constitutive models fit to biaxial tensile test data, here shown in atrial systole (*left*) and ventricular systole (*right*). The figure highlights the configurations of the mitral valve, including model chordae tendenae and papillary muscles, and the aortic valve. Transparent views are provided for the remaining structures of the heart and nearby great vessels.

great vessels. That modeling strategy facilitates incorporating experimentally constrained tissue mechanics models. Both models are derived from medical image data. With suitable validation, they promise to enable mechanistic simulations of cardiac physiology and pathophysiology for device design or treatment planning.

## 6. CONCLUSIONS

This review discussed the formulation of immersed methods for fluid–structure interaction and the application of these methods to selected biological and biomedical applications, but given the scope of the field, it is necessarily incomplete. For instance, there is active research that aims to improve the accuracy of immersed formulations while retaining the simplicity of the regularized delta function approach, including work by Stein et al. (2016, 2017). Other structural representations have also been introduced. For instance, Shankar et al. (2015) used radial basis functions, and Gil et al. (2010) developed a mesh-free structure discretization that tracks the displacement and deformation gradient of a system of marker points.

Immersed methods have also been used in other biological and biomedical modeling applications, including flows of cells and capsules (Eggleton & Popel 1998; Liu & Liu 2006; Fogelson & Guy 2008; Le 2010; Pranay et al. 2010, 2012; Crowl & Fogelson 2011; Fai et al. 2013, 2017; Zhu & Brandt 2015; Banaei et al. 2017; Saadat et al. 2018), cell migration and locomotion (Lewis et al. 2015, Li et al. 2017), insect flight (Miller & Peskin 2005, 2009; Bergou et al. 2007; Vargas et al. 2008), and phonation (Luo et al. 2008, Yang et al. 2017).

There is also substantial interest in adapting immersed methods to simulate Brownian particle systems by solving the equations of fluctuating hydrodynamics (FHD) together with rigid-body formulations (Sharma & Patankar 2004, Chen et al. 2006). For a single spherical particle in a fully periodic domain, it is possible to solve the overdamped problem through a Stokes version of the FHD equations (Sharma & Patankar 2004, Chen et al. 2006, Atzberger et al. 2007). In the case of multiple particles, special algorithms are required to account for the stochastic drift term appearing in the overdamped Langevin equation (Sprinkle et al. 2017a, 2019). These methods will facilitate simulations of microscale and nanoscale systems in which thermal fluctuations play a crucial role in the system dynamics, and they promise to enable the use of immersed methods in diverse applications in applied physics.

### SUMMARY POINTS

1. Immersed formulations of fluid–structure interaction allow for nonconforming discretizations of the fluid and structure. This avoids the frequent remeshing that is required by body-conforming discretization methods.
2. Modern immersed methods can be used with detailed elasticity models that can be parameterized using experimental data. Effective immersed methods have also been developed for models involving kinematic constraints.
3. Immersed methods using regularized delta functions are broadly applicable but lower-order accurate. Numerical methods based on the explicit treatment of jump conditions at fluid–structure interfaces yield improved accuracy, and recent versions of these methods enable the use of complex geometries.
4. These methods impact a range of applications in biology and medicine.

## FUTURE ISSUES

1. Adjoint pairs of Lagrangian–Eulerian coupling operators have not yet been developed for immersed interface methods, which limits their applicability in very low- and very high–Reynolds number applications.
2. Scalable linear and nonlinear solvers for implicit formulations are still lacking. These are needed to overcome severe time step size restrictions inherent in current explicit coupling schemes and will enable Brownian simulations in the overdamped limit.
3. Further research is needed to determine whether standard turbulence models can be used effectively with the formulations detailed herein, or if specialized turbulence models are required.
4. Further verification and validation studies are needed for the biomedical models to realize their full potential clinical impact.

## DISCLOSURE STATEMENT

The authors are not aware of any biases that might be perceived as affecting the objectivity of this review.

## ACKNOWLEDGMENTS

B.E.G. acknowledges research funding from NIH (National Institutes of Health) Awards R01HL117063 and U01HL143336 and NSF (National Science Foundation) Awards CBET 1757193, DMS 1664645, OAC 1450327, and OAC 1652541. He is grateful to Aleksandar Donev, David M. McQueen, and Charles S. Peskin for many collaborations and discussions on immersed boundary methods and related approaches to fluid–structure interaction. He also thanks Brent A. Craven, Alexander P. Hoover, Ebrahim M. Kolahdouz, Jae Ho Lee, David M. McQueen, Laura A. Miller, Charles S. Peskin, Charles Puelz, Simone Rossi, and Margaret Anne Smith in preparing simulation results and figures for this review. N.A.P. acknowledges research funding from NIH Award P01DK117824 and NSF Awards DMS 1418672 and OAC 1450374.

## LITERATURE CITED

Apte SV, Martin M, Patankar NA. 2009. A numerical method for fully resolved simulation (FRS) of rigid particle–flow interactions in complex flows. *J. Comput. Phys.* 228:2712–38

Atzberger PJ, Kramer PR, Peskin CS. 2007. A stochastic immersed boundary method for fluid-structure dynamics at microscopic length scales. *J. Comput. Phys.* 224:1255–92

Balboa Usabiaga F, Bell JB, Delgado-Buscalioni R, Donev A, Fai T, et al. 2012. Staggered schemes for fluctuating hydrodynamics. *Multiscale Model. Simul.* 10:1369–408

Balboa Usabiaga F, Kallemov B, Delmotte B, Bhalla APS, Griffith BE, Donev A. 2016. Hydrodynamics of suspensions of passive and active rigid particles: a rigid multiblob approach. *Comm. Appl. Math. Comput. Sci.* 11:217–96

Bale R, Hao M, Bhalla APS, Patankar NA. 2014a. Energy efficiency and allometry of movement of swimming and flying animals. *PNAS* 111:7517–21

Bale R, Hao M, Bhalla APS, Patel NK, Patankar NA. 2014b. Gray's paradox: a fluid mechanical perspective. *Sci. Rep.* 4:5904

Bale R, Neveln ID, Bhalla APS, MacIver MA, Patankar NA. 2015. Convergent evolution of mechanically optimal locomotion in aquatic invertebrates and vertebrates. *PLOS Biol.* 13:e1002123

Bale R, Shirgaonkar AA, Neveln ID, Bhalla APS, MacIver MA, Patankar NA. 2014c. Separability of drag and thrust in undulatory animals and machines. *Sci. Rep.* 4:7329

Banaei AA, Loiseau JC, Lashgari I, Brandt L. 2017. Numerical simulations of elastic capsules with nucleus in shear flow. *Eur. J. Comput. Mech.* 26:131–53

Bao Y, Kaye J, Peskin CS. 2016. A Gaussian-like immersed boundary kernel with three continuous derivatives and improved translational invariance. *J. Comput. Phys.* 316:139–44

Bazilevs Y, Calo VM, Hughes TJR, Zhang Y. 2008. Isogeometric fluid-structure interaction: theory, algorithms, and computations. *Comput. Mech.* 43:3–37

Bergou A, Xu S, Wang ZJ. 2007. Passive wing pitch reversal in insect flight. *J. Fluid Mech.* 591:321–37

Bhalla APS, Bale R, Griffith BE, Patankar NA. 2013. A unified mathematical framework and an adaptive numerical method for fluid-structure interaction with rigid, deforming, and elastic bodies. *J. Comput. Phys.* 250:446–76

Bischoff M, Wall WA, Bletzinger KU, Ramm E. 2004. Models and finite elements for thin-walled structures. In *Encyclopedia of Computational Mechanics*, Vol. 2, ed. E Stein, R de Borst, TJR Hughes, pp. 59–137. Hoboken, NJ: Wiley

Boffi D, Gastaldi L, Heltai L. 2018. A distributed Lagrange formulation of the finite element immersed boundary method for fluids interacting with compressible solids. In *Mathematical and Numerical Modeling of the Cardiovascular System and Applications*, ed. D Boffi, L Pavarino, G Rozza, S Scacchi, C Vergara, pp. 1–21. Cham, Switz.: Springer

Boffi D, Gastaldi L, Heltai L, Peskin CS. 2008. On the hyper-elastic formulation of the immersed boundary method. *Comput. Meth. Appl. Mech. Eng.* 197:2210–31

Bonet J, Gil AJ, Ortigosa R. 2015. A computational framework for polyconvex large strain elasticity. *Comput. Meth. Appl. Mech. Eng.* 283:1061–94

Borazjani I, Ge L, Sotiropoulos F. 2008. Curvilinear immersed boundary method for simulating fluid structure interaction with complex 3D rigid bodies. *J. Comput. Phys.* 227:7587–620

Borazjani I, Sotiropoulos F. 2008. Numerical investigation of the hydrodynamics of carangiform swimming in the transitional and inertial flow regimes. *J. Exp. Biol.* 211:1541–58

Borazjani I, Sotiropoulos F. 2009. Numerical investigation of the hydrodynamics of anguilliform swimming in the transitional and inertial flow regimes. *J. Exp. Biol.* 212:576–92

Casquero H, Zhang YJ, Bona-Casas C, Dalcin L, Gomez H. 2018. Non-body-fitted fluid–structure interaction: divergence-conforming B-splines, fully-implicit dynamics, and variational formulation. *J. Comput. Phys.* 374:625–53

Castell DO, Donner MW. 1987. Evaluation of dysphagia: a careful history is crucial. *Dysphagia* 2:65–71

Chen Y, Sharma N, Patankar N. 2006. Fluctuating Immersed Material (FIMAT) dynamics for the direct simulation of the brownian motion of particles. In *IUTAM Symposium on Computational Approaches to Multiphase Flow*, ed. S Balachandar, A Prosperetti, pp. 119–29. Dordrecht, Neth.: Springer

Colella P, Sekora MD. 2008. A limiter for PPM that preserves accuracy at smooth extrema. *J. Comput. Phys.* 227:7069–76

Cook IJ. 2008. Diagnostic evaluation of dysphagia. *Nat. Clin. Pract. Gastroenterol. Hepatol.* 5:393–403

Craven BA, Aycock KI, Manning KB. 2018. Steady flow in a patient-averaged inferior vena cava—part II: computational fluid dynamics verification and validation. *Cardiovasc. Eng. Technol.* 9:654–73

Crowl L, Fogelson AL. 2011. Analysis of mechanisms for platelet near-wall excess under arterial blood flow conditions. *J. Fluid Mech.* 676:348–75

Dasi LP, Ge L, Simon HA, Sotiropoulos F, Yoganathan AP. 2007. Vorticity dynamics of a bileaflet mechanical heart valve in an axisymmetric aorta. *Phys. Fluids* 19:067105

Devendran D, Peskin CS. 2012. An energy-based immersed boundary method for incompressible viscoelasticity. *J. Comput. Phys.* 231:4613–42

Donea J, Giuliani S, Halleux JP. 1982. An arbitrary Lagrangian-Eulerian finite element method for transient dynamic fluid-structure interactions. *Comput. Meth. Appl. Mech. Eng.* 33:689–723

Eggleton CD, Popel AS. 1998. Large deformation of red blood cell ghosts in a simple shear flow. *Phys. Fluids* 10:1834–45
Evans EA, Skalak R. 1980. *Mechanics and Thermodynamics of Biomembranes*. Boca Raton, FL: CRC
Fadlun EA, Verzicco R, Orlandi P, Mohd-Yusof J. 2000. Combined immersed-boundary finite-difference methods for three-dimensional complex flow simulations. *J. Comput. Phys.* 161:35–60
Fai TG, Griffith BE, Mori Y, Peskin CS. 2013. Immersed boundary method for variable viscosity and variable density problems using fast constant-coefficient linear solvers. I: numerical method and results. *SIAM J. Sci. Comput.* 35:B1132–61
Fai TG, Griffith BE, Mori Y, Peskin CS. 2014. Immersed boundary method for variable viscosity and variable density problems using fast constant-coefficient linear solvers. II: theory. *SIAM J. Sci. Comput.* 36:B589–621
Fai TG, Leo-Macias A, Stokes DL, Peksin CS. 2017. An image-based model of the spectrin cytoskeleton for red blood cell simulation. *PLOS Comput. Biol.* 11:e1005790
Fogelson AL, Guy RD. 2008. Immersed-boundary-type models of intravascular platelet aggregation. *Comput. Meth. Appl. Mech. Eng.* 197:2087–104
Gazzola M, Rees WMV, Koumoutsakos P. 2012. C-start: optimal start of larval fish. *J. Fluid Mech.* 698:5–18
Ge L, Dasi LP, Sotiropoulos F, Yoganathan AP. 2008. Characterization of hemodynamic forces induced by mechanical heart valves: Reynolds vs. viscous stresses. *Ann. Biomed. Eng.* 36:276–97
Ghosh SK, Kahrilas PJ, Zaki T, Pandolfino JE, Joehl RJ, Brasseur JG. 2005. The mechanical basis of impaired esophageal emptying postfundoplication. *Am. J. Physiol. Gastrointest. Liver Physiol.* 289:G21–35
Gil AJ, Carreño AA, Bonet J, Hassan O. 2010. The Immersed Structural Potential Method for haemodynamic applications. *J. Comput. Phys.* 229:8613–41
Gilmanov A, Sotiropoulos F. 2005. A hybrid Cartesian/immersed boundary method for simulating flows with 3D, geometrically complex, moving bodies. *J. Comput. Phys.* 207:457–92
Givelberg E. 2004. Modeling elastic shells immersed in fluid. *Comm. Pure Appl. Math.* 57:283–309
Glowinski R, Pan TW, Hesla TI, Joseph DD. 1999. A distributed Lagrange multiplier/fictitious domain method for particulate flows. *Int. J. Multiphase Flow* 25:755–94
Glowinski R, Pan TW, Periaux J. 1998. Distributed Lagrange multiplier methods for incompressible viscous flow around moving rigid bodies. *Comput. Meth. Appl. Mech. Eng.* 151:181–94
Griffith BE. 2009. An accurate and efficient method for the incompressible Navier–Stokes equations using the projection method as a preconditioner. *J. Comput. Phys.* 228:7565–95
Griffith BE. 2012. Immersed boundary model of aortic heart valve dynamics with physiological driving and loading conditions. *Int. J. Numer. Meth. Biomed. Eng.* 28:317–45
Griffith BE, Hornung RD, McQueen DM, Peskin CS. 2007. An adaptive, formally second order accurate version of the immersed boundary method. *J. Comput. Phys.* 223:10–49
Griffith BE, Hornung RD, McQueen DM, Peskin CS. 2009a. Parallel and adaptive simulation of cardiac fluid dynamics. In *Advanced Computational Infrastructures for Parallel and Distributed Adaptive Applications*, ed. M Parashar, X Li, pp. 105–30. Hoboken, NJ: Wiley
Griffith BE, Lim S. 2012. Simulating an elastic ring with bend and twist by an adaptive generalized immersed boundary method. *Comm. Comput. Phys.* 12:433–61
Griffith BE, Luo XY. 2017. Hybrid finite difference/finite element version of the immersed boundary method. *Int. J. Numer. Meth. Biomed. Eng.* 33:e2888
Griffith BE, Luo XY, McQueen DM, Peskin CS. 2009b. Simulating the fluid dynamics of natural and prosthetic heart valves using the immersed boundary method. *Int. J. Appl. Mech.* 1:137–77
Griffith BE, Peskin CS. 2005. On the order of accuracy of the immersed boundary method: higher order convergence rates for sufficiently smooth problems. *J. Comput. Phys.* 208:75–105
Guivier-Curien C, Deplano V, Bertrand E. 2009. Validation of a numerical 3-D fluid–structure interaction model for a prosthetic valve based on experimental PIV measurements. *Med. Eng. Phys.* 31:986–93
Holzapfel GA. 2000. *Nonlinear Solid Mechanics: A Continuum Approach for Engineering*. Hoboken, NJ: Wiley
Hoover AP, Griffith BE, Miller LA. 2017. Quantifying performance in the medusan mechanospace with an actively swimming three-dimensional jellyfish model. *J. Fluid Mech.* 813:1112–55

Hoover AP, Porras AJ, Miller LA. 2019. Pump or coast: the role of resonance and passive energy recapture in medusan swimming performance. *J. Fluid Mech.* 863:1031–61

Hsu MC, Kamensky D, Bazilevs Y, Sacks MS, Hughes TJR. 2014. Fluid–structure interaction analysis of bioprosthetic heart valves: significance of arterial wall deformation. *Comput. Mech.* 54:1055–71

Hsu MC, Kamensky D, Xu F, Kiendl J, Wang CL, et al. 2015. Dynamic and fluid–structure interaction simulations of bioprosthetic heart valves using parametric design with T-splines and Fung-type material models. *Comput. Mech.* 55:1211–25

Hu HH, Patankar NA, Zhu MY. 2001. Direct numerical simulations of fluid–solid systems using the arbitrary Lagrangian–Eulerian technique. *J. Comput. Phys.* 169:427–62

Hughes TJR, Cottrell JA, Bazilevs Y. 2005. Isogeometric analysis: CAD, finite elements, NURBS, exact geometry and mesh refinement. *Comput. Meth. Appl. Mech. Eng.* 194:4135–95

Iaccarino G, Verzicco R. 2003. Immersed boundary technique for turbulent flow simulations. *Appl. Mech. Rev.* 56:331–47

Jun BH, Saikrishnan N, Arjunon S, Yun BM, Yoganathan AP. 2014. Effect of hinge gap width of a St. Jude Medical bileaflet mechanical heart valve on blood damage potential—an in vitro micro particle image velocimetry study. *J. Biomech. Eng.* 136:091008

Kallemov B, Bhalla APS, Griffith BE, Donev A. 2016. An immersed boundary method for rigid bodies. *Comm. Appl. Math. Comput. Sci.* 11:79–141

Kamensky D, Hsu MC, Schillinger D, Evans JA, Aggarwal A, et al. 2015. An immersogeometric variational framework for fluid-structure interaction: application to bioprosthetic heart valves. *Comput. Meth. Appl. Mech. Eng.* 284:1005–53

Kern S, Koumoutsakos P. 2006. Simulations of optimized anguilliform swimming. *J. Exp. Biol.* 209:4841–57

Ketcheson DI, Parsani M, LeVeque RJ. 2013. High-order wave propagation algorithms for hyperbolic systems. *SIAM J. Sci. Comput.* 35:A351–77

Kim Y, Peskin CS. 2007. Penalty immersed boundary method for an elastic boundary with mass. *Phys. Fluids* 19:053103

Kim Y, Zhu L, Wang X, Peskin CS. 2003. On various techniques for computer simulation of boundaries with mass. In *Proceedings of the Second MIT Conference on Computational Fluid and Solid Mechanics*, ed. KJ Bathe, pp. 1746–50. Amsterdam: Elsevier

Kolahdouz EM, Bhalla APS, Craven BA, Griffith BE. 2019. An immersed interface method for discrete surfaces. *J. Comput. Phys.* In press

Kou W, Bhalla APS, Griffith BE, Pandolfino JE, Kahrilas PJ, Patankar NA. 2015a. A fully resolved active musculo-mechanical model for esophageal transport. *J. Comput. Phys.* 298:446–65

Kou W, Pandolfino JE, Kahrilas PJ, Patankar NA. 2015b. Simulation studies of circular muscle contraction, longitudinal muscle shortening, and their coordination in esophageal transport. *Am. J. Physiol. Gastrointest. Liver Physiol.* 309:G238–47

Kou W, Pandolfino JE, Kahrilas PJ, Patankar NA. 2017a. Could the peristaltic transition zone be caused by non-uniform esophageal muscle fiber architecture? A simulation study. *Neurogastroenterol. Motil.* 29:e13022

Kou W, Pandolfino JE, Kahrilas PJ, Patankar NA. 2017b. Simulation studies of the role of esophageal mucosa in bolus transport. *Biomechan. Model. Mechanobiol.* 16:1001–9

Kou W, Pandolfino JE, Kahrilas PJ, Patankar NA. 2018. Studies of abnormalities of the lower esophageal sphincter during esophageal emptying based on a fully coupled bolus-esophageal-gastric model. *Biomech. Model. Mechanobiol.* 17:1069–82

Lai MC, Li ZL. 2001. A remark on jump conditions for the three-dimensional Navier-Stokes equations involving an immersed moving membrane. *Appl. Math. Lett.* 14:149–54

Lai MC, Peskin CS. 2000. An immersed boundary method with formal second-order accuracy and reduced numerical viscosity. *J. Comput. Phys.* 160:705–19

Le DV. 2010. Subdivision elements for large deformation of liquid capsules enclosed by thin shells. *Comput. Meth. Appl. Mech. Eng.* 199:2622–32

Lee JH, Rygg AD, Kolahdouz EM, Rossi S, Retta SM, et al. 2019. Fluid–structure interaction models of an experimental pulse duplicator for simulating bioprosthetic heart valve dynamics. engrXiv 8ys2k. **https://doi.org/10.31224/osf.io/8ys2k**

Lewis OL, Zhang S, Guy RD, del Almo JC. 2015. Coordination of contractility, adhesion and flow in migrating *Physarum* amoebae. *J. R. Soc. Interface* 12:20141359

Li C, Qin B, Gopinath A, Arratia PE, Thomases B, Guy RD. 2017. Flagellar swimming in viscoelastic fluids: role of fluid elastic stress revealed by simulations based on experimental data. *J. R. Soc. Interface* 14:20170289

Li ZL, Lai MC. 2001. The immersed interface method for the Navier–Stokes equations with singular forces. *J. Comput. Phys.* 171:822–42

Lim S, Ferent A, Wang XS, Peskin CS. 2008. Dynamics of a closed rod with twist and bend in fluid. *SIAM J. Sci. Comput.* 31:273–302

Liu WK, Jun S, Zhang YF. 1995. Reproducing kernel particle methods. *Int. J. Numer. Meth. Fluids* 20:1071–106

Liu Y, Liu WK. 2006. Rheology of red blood cell aggregation by computer simulation. *J. Comput. Phys.* 220:139–54

Luo X, Mittal R, Zheng X, Bielamowicz SA, Walsh RJ, Hahn JK. 2008. An immersed-boundary method for flow–structure interaction in biological systems with application to phonation. *J. Comput. Phys.* 227:9303–32

MacIver MA, Fontaine E, Burdick JW. 2004. Designing future underwater vehicles: principles and mechanisms of the weakly electric fish. *IEEE J. Ocean. Eng.* 29:651–59

Maxian O, Kassen AT, Strychalski W. 2018. A continuous energy-based immersed boundary method for elastic shells. *J. Comput. Phys.* 271:333–62

McQueen DM, O'Donnell T, Griffith BE, Peskin CS. 2015. Constructing a patient-specific model heart from CT data. In *The Handbook of Biomedical Imaging: Methodologies and Clinical Research*, ed. N Paragios, J Duncan, N Ayache, pp. 183–97. New York: Springer

McQueen DM, Peskin CS. 1989. A three-dimensional computational method for blood flow in the heart. II. Contractile fibers. *J. Comput. Phys.* 82:289–97

McQueen DM, Peskin CS. 2000. A three-dimensional computer model of the human heart for studying cardiac fluid dynamics. *SIGGRAPH Comput. Graph.* 34:56–60

McQueen DM, Peskin CS. 2001. Heart simulation by an immersed boundary method with formal second-order accuracy and reduced numerical viscosity. In *Mechanics for a New Millennium: Proceedings of the 20th International Conference on Theoretical and Applied Mechanics (ICTAM 2000)*, ed. H Aref, JW Phillips, pp. 429–44. Dordrecht, Neth.: Springer

Miller LA, Peskin CS. 2005. A computational fluid dynamics of 'clap and fling' in the smallest insects. *J. Exp. Biol.* 208:195–212

Miller LA, Peskin CS. 2009. Flexible clap and fling in tiny insect flight. *J. Exp. Biol.* 212:3076–90

Mittal RK, Dong H, Bozkurttas M, Najjar FM, Vargas A, Von Loebbecke A. 2008. A versatile sharp interface immersed boundary method for incompressible flows with complex boundaries. *J. Comput. Phys.* 227:4825–52

Mittal RK, Iaccarino G. 2005. Immersed boundary methods. *Annu. Rev. Fluid Mech.* 37:239–61

Mittal RK, Padda B, Bhalla V, Bhargava V, Liu JM. 2006. Synchrony between circular and longitudinal muscle contractions during peristalsis in normal subjects. *Am. J. Physiol. Gastrointest. Liver Physiol.* 290:G431–38

Morinishi Y, Lund TS, Vasiyev OV, Moin P. 1998. Fully conservative higher order finite difference schemes for incompressible flow. *J. Comput. Phys.* 143:90–124

Nangia N, Bale R, Chen N, Hanna Y, Patankar NA. 2017a. Optimal specific wavelength for maximum thrust production in undulatory propulsion. *PLOS ONE* 12:e0179727

Nangia N, Johansen H, Patankar NA, Bhalla APS. 2017b. A moving control volume approach to computing hydrodynamic forces and torques on immersed bodies. *J. Comput. Phys.* 347:437–62

Nangia N, Patankar NA, Bhalla APS. 2019. A DLM immersed boundary method based wave-structure interaction solver for high density ratio multiphase flows. *J. Comput. Phys.* In press

Newren EP, Fogelson AL, Guy RD, Kirby RM. 2007. Unconditionally stable discretizations of the immersed boundary equations. *J. Comput. Phys.* 222:702–19

Nicosia MA, Brasseur JG. 2002. A mathematical model for estimating muscle tension in vivo during esophageal bolus transport. *J. Theor. Biol.* 219:235–55

Nobili M, Morbiducci U, Ponzini R, Del Gaudio C, Balducci A, et al. 2008. Numerical simulation of the dynamics of a bileaflet prosthetic heart valve using a fluid–structure interaction approach. *J. Biomech.* 41:2539–50

Nonaka A, May S, Almgren AS, Bell JB. 2011. A three-dimensional, unsplit Godunov method for scalar conservation laws. *SIAM J. Sci. Comput.* 33:2039–62

Patankar NA, Singh P, Joseph DD, Glowinski R, Pan TW. 2000. A new formulation of the distributed Lagrange multiplier/fictitious domain method for particulate flows. *Int. J. Multiphase Flow* 26:1509–24

Patel NK, Bhalla APS, Patankar NA. 2018. A new constraint-based formulation for hydrodynamically resolved computational neuromechanics of swimming animals. *J. Comput. Phys.* 375:684–716

Pearson K, Ekeberg O, Büschges A. 2006. Assessing sensory function in locomotor systems using neuromechanical simulations. *Trends Neurosci.* 29:625–31

Peskin CS. 1972. Flow patterns around heart valves: a numerical method. *J. Comput. Phys.* 10:252–71

Peskin CS. 1977. Numerical analysis of blood flow in the heart. *J. Comput. Phys.* 25:220–52

Peskin CS. 2002. The immersed boundary method. *Acta Numer.* 11:479–517

Peskin CS, McQueen DM. 1989. A three-dimensional computational method for blood flow in the heart. I. Immersed elastic fibers in a viscous incompressible fluid. *J. Comput. Phys.* 81:372–405

Peskin CS, McQueen DM. 1996. Fluid dynamics of the heart and its valves. In *Case Studies in Mathematical Modeling: Ecology, Physiology, and Cell Biology*, ed. HG Othmer, FR Adler, MA Lewis, JC Dallon, pp. 309–37. Englewood Cliffs, NJ: Prentice-Hall

Peskin CS, Printz BF. 1993. Improved volume conservation in the computation of flows with immersed elastic boundaries. *J. Comput. Phys.* 105:33–46

Pouderoux P, Lin S, Kahrilas PJ. 1997. Timing, propagation, coordination, and effect of esophageal shortening during peristalsis. *Gastroenterology* 112:1147–54

Pranay P, Anekal SG, Hernandez-Ortiz JP, Graham MD. 2010. Pair collisions of fluid-filled elastic capsules in shear flow: effects of membrane properties and polymer additives. *Phys. Fluids* 22:123103

Pranay P, Henríquez-Rivera RG, Graham MD. 2012. Depletion layer formation in suspensions of elastic capsules in Newtonian and viscoelastic fluids. *Phys. Fluids* 24:061902

Quaini A, Canic S, Glowinski R, Igo S, Hartley CJ, et al. 2012. Validation of a 3D computational fluid–structure interaction model simulating flow through an elastic aperture. *J. Biomech.* 45:310–18

Roy S, Heltai L, Costanzo F. 2015. Benchmarking the immersed finite element method for fluid-structure interaction problems. *Comput. Math. Appl.* 69(10):1167–88

Saadat A, Guido CJ, Iaccarino G, Shaqfeh ESG. 2018. Immersed-finite-element method for deformable particle suspensions in viscous and viscoelastic media. *Phys. Rev. E* 98:063316

Shankar V, Wright GB, Kirby RM, Fogelson AL. 2015. Augmenting the immersed boundary method with Radial Basis Functions (RBFs) for the modeling of platelets in hemodynamic flows. *Int. J. Numer. Meth. Fluids* 79:536–57

Sharma N, Patankar NA. 2004. Direct numerical simulation of the Brownian motion of particles by using fluctuating hydrodynamic equations. *J. Comput. Phys.* 201:466–86

Sharma N, Patankar NA. 2005. A fast computation technique for the direct numerical simulation of rigid particulate flows. *J. Comput. Phys.* 205:439–57

Shirgaonkar AA, Curet OM, Patankar NA, MacIver MA. 2008. The hydrodynamics of ribbon-fin propulsion during impulsive motion. *J. Exp. Biol.* 211:3490–503

Shirgaonkar AA, MacIver MA, Patankar NA. 2009. A new mathematical formulation and fast algorithm for fully resolved simulation of self-propulsion. *J. Comput. Phys.* 228:2366–90

Siguenza J, Pott D, Mendez S, Sonntag SJ, Kaufmann TAS, et al. 2018. Fluid-structure interaction of a pulsatile flow with an aortic valve model: a combined experimental and numerical study. *Int. J. Numer. Methods Biomed. Eng.* 34:e2945

Sprinkle B, Balboa Usabiaga F, Patankar NA, Donev A. 2017a. Large scale Brownian dynamics of confined suspensions of rigid particles. *J. Chem. Phys.* 147:244103

Sprinkle B, Bale R, Bhalla APS, MacIver MA, Patankar NA. 2017b. Hydrodynamic optimality of balistiform and gymnotiform locomotion. *Eur. J. Comput. Mech.* 26:31–43
Sprinkle B, Donev A, Bhalla APS, Patankar NA. 2019. Brownian dynamics of fully confined suspensions of rigid particles without Green's functions. *J. Chem. Phys.* 150:164116
Stein DB, Guy RD, Thomases B. 2016. Immersed boundary smooth extension: a high-order method for solving PDE on arbitrary smooth domains using Fourier spectral methods. *J. Comput. Phys.* 304:252–74
Stein DB, Guy RD, Thomases B. 2017. Immersed Boundary Smooth Extension (IBSE): a high-order method for solving incompressible flows in arbitrary smooth domains. *J. Comput. Phys.* 335:155–78
Stockie JA. 2009. Modelling and simulation of porous immersed boundaries. *Comput. Struct.* 87:701–9
Taira K, Colonius T. 2007. The immersed boundary method: a projection approach. *J. Comput. Phys.* 225:2118–37
Tango AM, Salmonsmith J, Ducci A, Burriesci G. 2018. Validation and extension of a fluid–structure interaction model of the healthy aortic valve. *Cardiovasc. Eng. Technol.* 9:739–51
Taylor GK, Nudds RL, Thomas AL. 2003. Flying and swimming animals cruise at a Strouhal number tuned for high power efficiency. *Nature* 425:707–11
Tytell ED, Hsu CY, Williams TL, Cohen AH, Fauci LJ. 2010. Interactions between internal forces, body stiffness, and fluid environment in a neuromechanical model of lamprey swimming. *PNAS* 107:19832–37
Udaykumar HS, Mittal R, Rampunggoon P, Khanna A. 2001. A sharp interface Cartesian Grid method for simulating flows with complex moving boundaries. *J. Comput. Phys.* 174:345–80
Vadala-Roth B, Rossi S, Griffith BE. 2018. Stabilization approaches for the hyperelastic immersed boundary method for problems of large-deformation incompressible elasticity. arXiv:1811.06620 [math.NA]
van Rees WM, Gazzola M, Koumoutsakos P. 2013. Optimal shapes for anguilliform swimmers at intermediate Reynolds numbers. *J. Fluid Mech.* 722:R3
Vargas A, Mittal R, Dong H. 2008. A computational study of the aerodynamic performance of a dragonfly wing section in gliding flight. *Bioinspir. Biomim.* 3:026004
Verma S, Novati G, Koumoutsakos P. 2018. Efficient collective swimming by harnessing vortices through deep reinforcement learning. *PNAS* 115:5849–54
Votta E, Le TB, Stevanella M, Fusini L, Caiani EG, et al. 2013. Toward patient-specific simulations of cardiac valves: state-of-the-art and future directions. *J. Biomech.* 46:217–28
Wang X, Zhang LT. 2010. Interpolation functions in the immersed boundary and finite element methods. *Comput. Mech.* 45:321–34
Webb PW. 1984. Form and function in fish swimming. *Sci. Am.* 251:58–68
Wheeler JB, Reed CE. 2012. Epidemiology of esophageal cancer. *Surg. Clin. North Am.* 92:1077–87
Wu MCH, Zakerzadeh R, Kamensky D, Kiendl J, Sacks MS, Hsu MC. 2018. An anisotropic constitutive model for immersogeometric fluid–structure interaction analysis of bioprosthetic heart valves. *J. Biomech.* 74:23–31
Wu W, Pott D, Mazza B, Sironi T, Dordoni E, et al. 2016. Fluid–structure interaction model of a percutaneous aortic valve: comparison with an *in vitro* test and feasibility study in a patient-specific case. *Ann. Biomed. Eng.* 44:590–603
Xu F, Morganti S, Zakerzadeh R, Kamensky D, Auricchio F, et al. 2018. A framework for designing patient-specific bio-prosthetic heart valves using immersogeometric fluid–structure interaction analysis. *Int. J. Numer. Methods Biomed. Eng.* 34:e2938
Xu S, Wang ZJ. 2006a. An immersed interface method for simulating the interaction of a fluid with moving boundaries. *J. Comput. Phys.* 216:454–93
Xu S, Wang ZJ. 2006b. Systematic derivation of jump conditions for the immersed interface method in three-dimensional flow simulation. *SIAM J. Sci. Comput.* 27:1948–80
Xu S, Wang ZJ. 2008. A 3D immersed interface method for fluid-solid interaction. *Comput. Meth. Appl. Mech. Eng.* 197:2068–86
Yang J, Wang X, Krane M, Zhang LT. 2017. Fully-coupled aeroelastic simulation with fluid compressibility—for application to vocal fold vibration. *Comput. Meth. Appl. Mech. Eng.* 315:584–606

Ye T, Mittal R, Udaykumar HS, Shyy W. 1999. An accurate Cartesian grid method for viscous incompressible flows with complex immersed boundaries. *J. Comput. Phys.* 156:209–40

Zhang L, Gerstenberger A, Wang X, Liu WK. 2004. Immersed finite element method. *Comput. Meth. Appl. Mech. Eng.* 193:2051–67

Zhao H, Freund JB, Moser RD. 2008. A fixed-mesh method for incompressible flow-structure systems with finite solid deformations. *J. Comput. Phys.* 227:3114–40

Zhu L, Brandt L. 2015. The motion of a deforming capsule through a corner. *J. Fluid Mech.* 770:374–97

Zhu L, Peskin CS. 2002. Simulation of a flapping flexible filament in a flowing soap film by the immersed boundary method. *J. Comput. Phys.* 179:452–68